https://doi.org/10.5194/egusphere-2024-4074
Preprint. Discussion started: 17 February 2025

Measurement report: Microphysical and optical characteristic of radiation fog - a study using in-situ, remote sensing, and balloon techniques.

Katarzyna Nurowska[1,2], Przemysław Makuch[3], and Krzysztof M. Markowicz[1]

[1]University of Warsaw, Faculty of Physics, Institute of Geophysics
[2]Guangdong Technion - Israel Institute of Technology, Department of Mathematics
[3]Polish Academy of Sciences, Institute of Oceanology

Correspondence: Katarzyna Nurowska (Katarzyna.Nurowska@fuw.edu.pl)

Abstract. This study investigates the vertical profiles of microphysical and thermodynamic properties within radiative fog layers in the Strzyżów valley (Southeastern Poland), based on in-situ, remote sensing and tethered balloon soundings data. Across three case studies of radiation fog that occurred in September 2023, 74 soundings were performed, with 41 employing the OPC-N3 instrument to capture droplet spectra. The results indicated similar weather conditions in all cases, with a liquid water path consistently above 15 g·m^{-2}, although no transition to dense fog was observed. The effective droplet radius decreased with height (between 3-4.6 μm for 100 m), with larger droplets ($\geq$18.5 μm) concentrated near the ground.

The fog dissipated both from the top and bottom, with the mature fog stage marked by peak liquid water content (LWC) and the droplet number concentration (N_c) near 80% of the fog height. Theoretical calculations of droplet terminal velocity (for droplets $\geq$18.5 μm) indicate that larger droplets are removed from fog layers within minutes, affecting the longevity of the fog. Equivalent adiabaticity values (α_{eq} - the ratio by which the adiabatic lapse rate of the mixing ratio needs to be multiplied to give the same amount of liquid water path as observed in a specific cloud) ranged between 0 and 0.6. Except in one instance where negative values α_{eq} were observed near the ground, a phenomenon scarcely reported in existing fog studies.

Having instruments measuring radiation at two different heights, it was possible to estimate the effect of fog on reducing the total shortwave and longwave (NET) radiation at ground level by 150 W·m^{-2} (just before the fog disappearing and after). The measured dependence of the reduction of longwave radiation by fog depends linearly on the amount of liquid water path.

As a result of the measurements, average values of liquid water content and droplet number concentrations were obtained for the observed optically thin fogs in the valley area. Mean LWC in the fog layer core was found between 0.2–0.4 g·m^{-3}, with N_c up to 300 cm^{-3}. The effective radius (8–10 μm) exhibited a linear height-dependent decrease, with radiation model closures yielding minimal biases, supporting the accuracy of radiation assessments within fog environments.

1 Introduction

A characteristic feature of radiation fogs is their localized nature, as they do not cover large areas, making their forecasting challenging. Weather conditions contribute to approximately 30% of aviation accidents in the USA Gultepe (2023). Radiation

https://doi.org/10.5194/egusphere-2024-4074
Preprint. Discussion started: 17 February 2025

fog significantly reduces visibility and complicates navigation, posing a threat to transportation. According to the American National Transportation Safety Board (NTSB), fog is the second most critical weather-related factor leading to fatal aviation accidents, accounting for an estimated 14% of such incidents Capobianco and Lee (2001). Fog impacts not only safety but also causes economic damage. It can lead to road traffic disruptions, sounding cancellations, and airport closures. Based on the NTSB analysis, visibility-related effects contribute to aircraft-related delays approximately 30-35% of the time Gultepe et al. (2019).

Fog is a meteorological phenomenon occurring near the Earth's surface, characterized by the suspension of water droplets in the air, significantly reducing visibility to below 1 km George (1951). Several types of fog exist, depending on their formation mechanisms. This article focuses on radiation fog, which primarily forms at night under clear-sky and minimal wind conditions, within a stable boundary layer (SBL). Under such conditions, the ground surface cools significantly, leading to the cooling of the air immediately above it Lakra and Avishek (2022). Once the dew point temperature is reached, water vapor condenses on suspended particles (condensation nuclei), forming fog. This type of fog develops from the ground upwards, usually not exceeding 200 meters in height. The cooling of successive air layers occurs from the lower layer upward, which is why radiation fogs are associated with the formation of temperature inversions. After sunrise, and with the onset of stronger winds, the fog and the inversion dissipate. When radiation fog forms, it initially remains optically thin to longwave (LW) radiation and develops within a stable lapse rate. When fog becomes optically thick, cooling occurs predominantly at the top of the fog layer, while the portion near the ground radiates in LW range that is able to warm the surface Mason (1982); Price (2011). The potential equivalent temperature becomes uniform throughout the fog layer, inducing slight instability, which in turn increases turbulence within the fog. As demonstrated by Price (2011), approximately 50% of the fog cases he analyzed transitioned into optically thick, well-mixed fogs characterized by a saturated adiabatic stability profile. His research suggests that this conversion typically occurs when the fog layer exceeds 100 meters in thickness. Numerical weather models have difficulty catching the shift from optically thin to optically thick layer Poku et al. (2021); Boutle et al. (2022); Antoine et al. (2023).

The Costabloz et al. (2024) studied fog development during SOFOG3D experiment. They proposed several methods for establishing if when occurs the transition from thin to optically thick fog:

- surface LW net radiation should approach to 0. In their research they assumed that this condition occurs when $|\Delta \mathrm{LW}| < 5$ $\mathrm{W \cdot m^{-2}}$
- profile of air temperature (T) decreases with height, due to warming the surface and cooling at the top of fog. They were checking this condition if T at 50 m is lower than T at 25 m.
- turbulent kinetic energy exceeds 0.10 $\mathrm{m^2 \cdot s^{-2}}$,
- fog top height exceeds 110 m,
- Wærsted et al. (2017) proposed LWP< 30 $\mathrm{g \cdot m^{-2}}$, however Costabloz et al. (2024) found that in SOFOG3D experiment this value is too high. They proposed that LWP > 15 $\mathrm{g \cdot m^{-2}}$, so it more matches the time when other criteria are met.

Those conditions were met in SOFOG3D experiment closely in time within around 1 hour.

https://doi.org/10.5194/egusphere-2024-4074
Preprint. Discussion started: 17 February 2025

Key factors influencing the likelihood of fog transitioning into an optically thick state include the time of its formation (the more time before sunrise, the better) and the humidity profile of the air Boutle et al. (2018). For droplets to begin forming, aerosols acting as cloud condensation nuclei (CCN), such as for example ammonium nitrate aerosols, are required. In clouds, turbulence can uplift air masses, activating CCNs more rapidly and extensively. In fog, droplet growth is primarily governed by radiative cooling. As demonstrated by Boutle et al. (2018), a higher concentration of large aerosol particles accelerates the transition to a well-mixed fog state. Additionally, the type of aerosol present in the air is important; compounds with high hygroscopicity that can activate at low supersaturation levels are most effective as CCN Gilardoni et al. (2014).

According to Costabloz et al. (2024), during SOFOG3D, inverted LWC profiles—maximum LWC found at the ground and decreasing with altitude—were commonplace in optically thin fogs. Mostly in well-mixed optically thick fogs, quasi-adiabatic profiles with LWC increasing with height were found. However in one case they measured LWC profiles decreasing with height one hour after the transition occurred and LWC values at the ground reached 0.25 g.m-3, the highest values recorded during whole campaign.

Research utilizing cloud radars, ceilometers, and microwave radiometers has established the rate at which LW radiative cooling can produce water within fog. For fogs with a liquid water path (LWP) exceeding 30 $g{\cdot}m^{-2}$ under clear-sky, this rate is approximately 70 $g{\cdot}m^{-2}{\cdot}h^{-1}$ Wærsted et al. (2017). The presence of clouds above the fog can also influence water condensation, with low clouds potentially blocking cooling entirely, leading to fog dissipation.

After sunrise, shortwave (SW) radiation begins to heat the fog, causing droplet evaporation. Wærsted et al. (2017) estimated that the strength of this process is about 10-15 $g{\cdot}m^{-2}{\cdot}h^{-1}$. The rate of evaporation increases with the effective radius of droplets (r_{eff}) and LWP, and decreases with larger solar zenith angles. Additionally, the warming of the ground surface transfers approximately 30 $g{\cdot}m^{-2}{\cdot}h^{-1}$ of sensible heat to the fog.

To accurately predict the formation and evolution of fog, a weather forecasting model must effectively represent the interactions between the atmosphere and the Earth's surface, various processes (such as microphysics, radiation, and turbulence), and it must do so on a local scale while accounting for terrain features.

One approach to studying fog is through large-eddy simulations (LES) modeling. This approach enables the examination of turbulence effects and interactions between the atmosphere and the surface Maronga and Bosveld (2017), the deposition of droplets on vegetation Mazoyer et al. (2017), or the influence of the urban canopy Bergot et al. (2015) on fog formation and evolution. Numerical models often struggle to accurately forecast fog formation, dissipation, depth, or water content Román-Cascón et al. (2012); Zhou et al. (2012); Bari et al. (2023). This difficulty arises from the fog's localized nature and the delicate balance between processes such as radiation balance, droplet deposition on the surface, turbulent mixing, microphysical properties, and moisture availability. Recently, AI-based tools, including machine learning and deep learning, have been employed to enhance numerical weather prediction (NWP). While these methods have shown promising results, they also introduce new challenges. Machine learning requires high-quality datasets specific to each forecast location, as well as substantial computational resources to produce timely results Bari et al. (2023).

For the initialization of numerical models or the development of methods to retrieve LWP from satellites, it is essential to understand the microphysical properties of fog as a function of height. Unfortunately, there is a scarcity of data on the

https://doi.org/10.5194/egusphere-2024-4074
Preprint. Discussion started: 17 February 2025

vertical distribution of fog's microphysical characteristics. Measurements using aircraft are impractical because fog typically forms close to the Earth's surface and inherently reduces visibility. However, measurements can be conducted using aerological balloons Egli et al. (2015), instrumentation placed on tall towers Ye et al. (2015); Han et al. (2018), and more recently, drones and microwave radiometers (MWR) have become viable options for such observations.

Using a tethered balloon, Pinnick et al. (1978) made the first measurements of the vertical profiles of microphysical characteristics in fog. He showed that in the studied cases a fog had a bimodal distribution of droplets (r=5 μm and r=0.6 μm) with LWC range from 10^{-4} to 0.45 g·m^{-3}.

Egli et al. (2015) performed soundings with tethered balloon, and measured LWC, N_c and r_{eff} every 10 m. His results from two fog cases show that the changes in LWC are related to the change in N_c and not to the change in droplet size. In most cases, r_{eff} was constant with height. One fog case was characterised by low LWC (maximum of 0.14 g·m^{-3}) however high N_c above 2000 cm^{-3}. In this case of fog, 3 measurements were taken. Omitting the values of r_{eff} at the very bottom of the profiles (where the values dropped significantly), the value of r_{eff} decreased with height. In the case of one profile, the value of $_{eff}$ at a 25 m reached a maximum of 9.4 μm. Second fog case, within six soundings, consist of a considerably thicker fog with higher LWC and r_{eff} values, although accompanied by lower total drop counts. LWC had a constant pattern in the first third of the height, then LWC increased with height and then decreased with height to the cloud top. The highest LWC value was 0.54 g·m^{-3}. N_c had a similar pattern with height as LWC. The highest N_c value recorded was 500 cm^{-3}. The r_{eff} values differ from sounding to sounding, however were constant with height, in range between 4 and 8 μm.

The motivation for this study is the miniaturization of equipment for particle detection. For example, the OPC-N3 sensor, commonly used for aerosol monitoring, can also be used to measure the microphysical properties of fog when mounted on a tethered balloon or drone (Nurowska et al. (2023)). Such a system was employed to capture vertical profiles of radiative fog in a mountain valley, a region where air pollution can be elevated during inversion conditions. This type of terrain enables fog monitoring at different altitudes. In this setup, SW and LW radiometers positioned near the valley bottom and mountain top allow for determining the optical, microphysical, and radiation closure of the fog. Section 2 outlines the instruments utilized for conducting the measurements, while Section 3 details the methodology of the in-situ measurements and the model setup. The core of the article is presented in Section 4, which features a case study of radiative fog occurrence, including optical, microphysical, and radiation closure analyses performed for this case. Section 4 focuses on an event in the Strzyżów valley, where data were gathered using a balloon. The 1D Fu-Liou radiative transfer model was applied to simulate the conditions in the Strzyżów valley, incorporating additional data from the SolarAOT station (which consists of an upper and lower station).

2 Experiment setup

This study is based on measurements taken at two sites in the Strzyżów. This a small town is located in Southern Poland in region of Strzyżowskie Foothills. The city is located next to the river Wisłok. The research was conducted using remote sensing and in-situ techniques as well as by apparatus connected to a tethered balloon. In addition, numerical stimulation were used for radiation closure study.

https://doi.org/10.5194/egusphere-2024-4074
Preprint. Discussion started: 17 February 2025

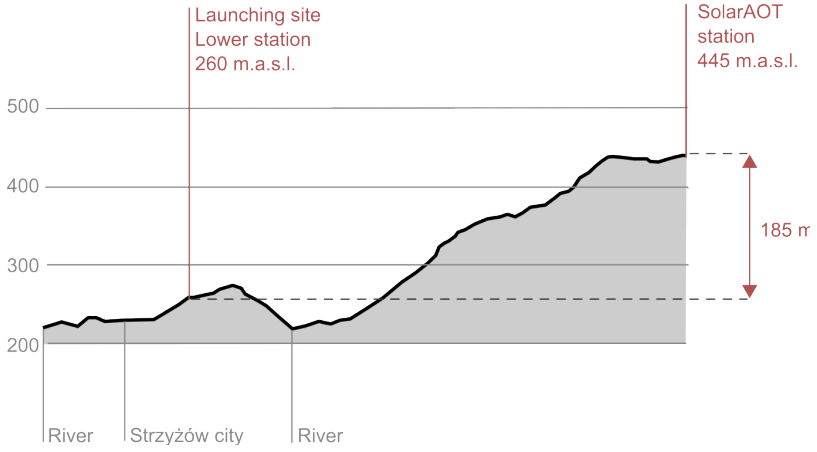

Figure 1. Location of tethered balloon launching site SolarAOT$_{lower}$ and SolarAOT^{upper} station, in relation to the Strzyżów city and the Wisłok river.

2.1 SolarAOT^{upper} station

The balloon launching site was located on a slope of a hill at 260 m a.s.l. of valley of Strzyżów city. Next to the town is situated a SolarAOT - a private radiative transfer research station which collaborates with University of Warsaw. The location of both stations is shown on Fig. 1.

SolarAOT^{upper} is a private radiative transfer research station (collaborates with University of Warsaw) is located in an agricultural area on one of the peaks of the Niebylecka Mountain on 445 m a.s.l. (49°52'43.0"N 21°51'40.8"E), located from Strzyżów city in straight line 4 km, vertical height difference 185 m. At the station are mounted several instruments, inter alia, pyranometer CMP21, Eppley pyrgeometer, CIMEL, Nephelometer Aurora 4000, Aethalometr AE-31, CHM-15K ceilometr, lidar, and RPG-HATPRO-G5. CIMEL is an instrument for measuring direct and scattered solar radiation in 9 spectral channels: 340, 380, 440, 500, 675, 870, 936, 1020, 1640 nm. Based on the measured values, the optical parameters of the aerosol are determined, including the AOD or the Angstrom exponent. The data collected by the instrument is processed within the international AERONET measurement network. Nephelometer Aurora 4000 is used to measure light scattering coefficients on aerosols for wavelengths of 450, 525, 630 nm in 18 ranges of aerosol scattering angles. Aethalometr AE-31 is used to measure the concentration of equivalent of black carbon (eBC) in the atmosphere and the aerosol absorption coefficient of the aerosol. The measurement is performed at 7 wavelengths (370, 470, 520, 590, 660, 880, 950 nm) using the method of changing the transmission of a quartz filter on which the aerosol is deposited.

2.2 SolarAOT$_{lower}$ - launching site

The lower station is located at valley of Strzyżów city at 260 m.a.s.l. (49°52'18.0"N 21°48'26.0"E). On the site of balloon lunching there was mounted CNR4 net radiometer for upward and downward SW and LW flux; meteo station including MetPak

https://doi.org/10.5194/egusphere-2024-4074
Preprint. Discussion started: 17 February 2025

and sensors A100LK, W200P, HYT936, OPC-N3. In addition, the mobile laboratory equipped with Aurora 4000 nephelometer, Laser Aerosol Spectrometer LAS 3340A, and Oxford Lasers VisiSize D30 (ShadowGraph) was used at this site. Raymetrics single wavelength (532 nm) lidar 510M for aerosol and cloud detection was used.

The VisiSize D30 system, developed by Oxford Lasers Ltd., operates using the shadowgraph technique. The VisiSize D30, hereafter referred to as ShadowGraph, captures shadow images of particles as they pass through the measurement volume between a laser head and a high-resolution camera. This system enables the determination of microphysical properties, including particle shape, size, droplet size distribution (DSD(r)), total droplet number concentration, and liquid water content (LWC).

The ShadowGraph system has been effectively utilized in the study of cloud microphysics, both in laboratory settings and during in situ measurements. The droplet detection and sizing mechanisms of the ShadowGraph were comprehensively detailed by Nowak et al. (2021). Data collected using the ShadowGraph in studies of orographic clouds, specifically under foggy conditions in mountainous regions, were analyzed by Mohammadi et al. (2022). In our measurements we treat this instrument as reference instrument to which are calibrated OPC-N3, as have been showed in article Nurowska et al. (2023).

2.3 Balloon apparatus

For measurements were used two meteorological balloons filled with helium. Balloon was tethered using the Vaisala TTW111 Winch (see Figure 2a). Around two meters below balloon the apparatus was mounted on the rope holding the balloon. The set up used at the balloon was (see Figure 2b):

- Vaisala radiosonde RS41 - collecting data about pressure (p), T, relative humidity (RH),
- GY-63 MS5611 - a high performance pressure sensor module,
- HYT 939 - additional T and realtive humidity sensor,
- Alphasense OPC-N3 - optical particle matter (PM) sensor that measures mass concentration in size range [1] $PM_{1.0}$, $PM_{2.5}$ and PM_{10} mass concentration, however here was used to gather the data about fog droplets based on article Nurowska et al. (2023).
- SENSIRION SPS30 - optical PM sensor that measures $PM_{1.0}$, $PM_{2.5}$ PM_4, PM_{10} mass concentration
- TFMini - visibility sensor
- AE-51 - miniature aethalometer for measuring the eBC concentration and the aerosol absorption coefficient at a wavelength of 880 nm.

not all the time the radiosonde, AE-51 was present - due to the weight of the balloon and its buoyancy.

The OPC-N3, an optical particle counter designed by Alphasense Ltd., utilizes a diode laser emitting light at a wavelength of 658 nm, along with an elliptical mirror that directs the laser beam towards a detector. The airflow, driven perpendicularly to the

[1] number after PM denotes size range up to this size in μm

https://doi.org/10.5194/egusphere-2024-4074
Preprint. Discussion started: 17 February 2025

(a) Balloon with attached payload and connected to the winch.

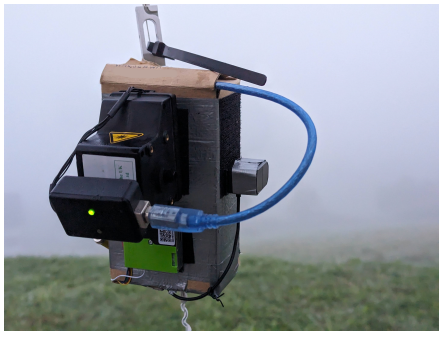

(b) Zoom to the balloon payload, showing: inside the box (GY-63, HYT 939), OPC-N3, SPS30, TFMini

Figure 2. Balloon setup.

laser beam by an integrated fan, allows for continuous operation. The OPC-N3 quantifies particle number concentration (NC) across 24 size bins, covering a diameter range from 0.35 to 40 μm. The onboard algorithm converts NC measurements into PM1, PM2.5, and PM10 values. Detailed specifications of the OPC-N3 is available in the work by Hagan and Kroll (2020).

3 Methodology and model set up

3.1 Balloon measurements methodology

For three days between 9 - 11 September 2023 the measurements of radiative fog were held in Strzyżów city, Poland. The balloon launch site was located in the valley of Strzyżów city. Two meteorological balloons (for better buoyancy) filled with helium (to around 1,5 m diameter) were tethered using the Vaisala TTW111 Winch. Below the balloons was attached apparatus to the winch rope. Four setups were used, as it was not possible due to the buoyancy to mount all instruments at once:

- setup 1: GY-63, HYT 939, OPC-N3, SPS30, TTFMini - this setup was most common
- setup 2: only Vaisala radiosonde RS41
- setup 3: Vaisala radiosonde RS41, AE-51.
- setup 4: Vaisala radiosonde RS41, GY-63, HYT 939, OPC-N3, SPS30, TFMini

Figure 3 shows with colored lines when during the night the soundings were done, with colors are indicated different setups mounted on the balloon. The same information but with specific sounding times can be found in the Appendix A1. In total there were 74 soundings, however due to problems with data recording 11 soundings are missing all or some data and were not taken into account in further analysis (marked in Figure 3 and Table A1 in gray). Sounding were done by unwinding the rope until it started to tilt to horizon. The balloon was stopped for few seconds, and the line was wound up. Soundings were done with around 15 minutes brakes in between.

https://doi.org/10.5194/egusphere-2024-4074
Preprint. Discussion started: 17 February 2025

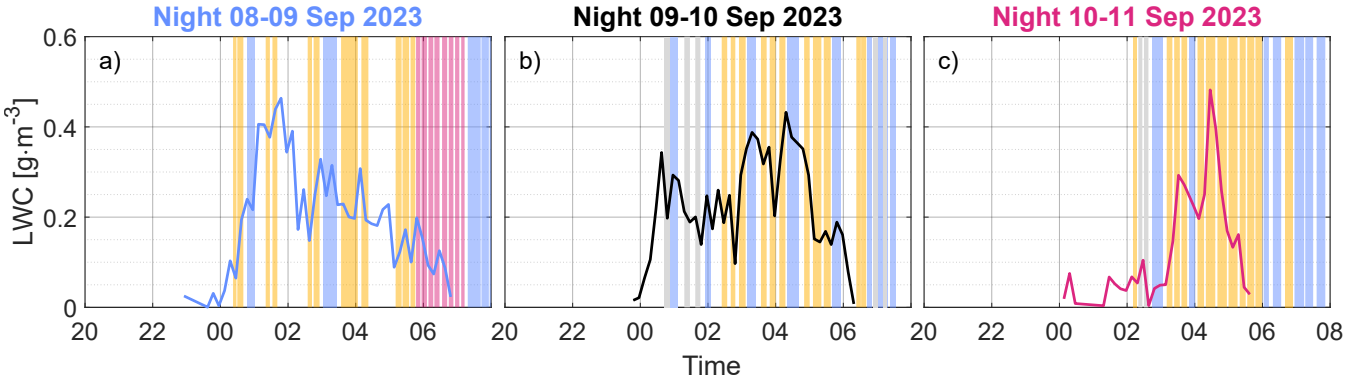

Figure 3. Figure visualize when the soundings where done, colors presents what apparatus was mounted on the balloon: orange - setup with OPC-N3, blue - setup with radiosonde, pink - setup with OPC-N3 and radiosonde, gray - problems with collected data. The image is overlaid on the line representing temporal variability of the LWC at the ground obtained from Shadowgraph (the same figure as on 5.

Fog episode		Stage		
		Initial	Developed	Decaying (soundings after fog vanishing)
Night 8-9	Time	23:00 - 2:34	2:34 - 6:42	6:45 - 7:00 (8:10)
	Profiles with OPC-N3	4	12	2(+1)
	Profiles with Radiosonde	1	6	2 (+4)
Night 9-10	Time	00:00 - 2:45	2:45 - 6:00	6:00 - 7:30
	Profiles with OPC-N3	0	9	2
	Profiles with Radiosonde	1	4	3
Night 10-11	Time	2:00 - 3:02	3:02 - 5:30	5:30 - 6:00 (8:00)
	Profiles with OPC-N3	1	7	2 (+1)
	Profiles with Radiosonde	1	2	0 (+5)

Table 1. Times of initial, developed and decaying stage of observed fogs on days 9 - 11 Sep. with information on how many soundings were performed in each period.

The fog case description was divided into 3 phases: initial, developed and decaying. The transition from initial phase to developed was assumed to occur when LWP>15 g·m^{-2}, the change from mature to decaying was assumed when LWP<15 g·m^{-2}.

Table 1 presents information about each fog stage.

During campaign ShadowGraph was used for two purposes, one to calibrate OPC-N3 and other to monitor situation near surface. As ShadowGraph works on the basis of a considerable power laser with invisible to the human eye light, for safety purposes, it was placed on the roof of the mobile laboratory at a height of approx. 3 m above the ground. OPC-N3 was used measure the N_c; the r_{eff} and the LWC. OPC-N3 was calibrated to the ShadowGraph following Nurowska et al. (2023). Results of $NC_{droplets}$, LWC and r_{eff} were obtained by taking bins of OPC-N3 measuring particles grater than 1.15 μm (bin 7 of OPC-N3).

https://doi.org/10.5194/egusphere-2024-4074
Preprint. Discussion started: 17 February 2025

The calibration equations between used OPC-N3 and Shadowgraph are:

$$\mathrm{LWC_{ShadowGraph}} = 6.15 \cdot \mathrm{LWC_{OPC\text{-}N3}} + 0.11 \tag{1}$$

$$\mathrm{N_{cShadowGraph}} = 4.16 \cdot \mathrm{N_{cOPC\text{-}N3}} + 32.63 \tag{2}$$

$$\mathrm{r_{eff}^{ShadowGraph}} = 0.70 \cdot \mathrm{r_{eff}^{OPC\text{-}N3}} + 3.81 \tag{3}$$

One sounding consisted of launching the balloon, at some point the balloon was no more going upward (but started to move horizontally) then the winch was stopped and started to wind up the winch string. During one balloon launch, we obtained two vertical profiles, which were then averaged over height to obtain an image less noisy by random fluctuations. All the data were interpolated every 1 m for making figures. On the plots soundings starts at 2 m above ground.

The OPC-N3 allows to calculate volume droplet size distribution (vDSD) which can be computed using formula:

$$\mathrm{vDSD}(r_b) = N_b \cdot (\Delta r_b \cdot V_b)^{-1} \cdot r_b^3 \tag{4}$$

where N_b is the number of droplets in a bin, V_b the volume of a bin, Δr_b the width of the bin and r_b the mean bin droplet radius. The obtained vDSD was not calibrated with ShadowGraph. vDSD gives information which droplets give biggest contribution to LWC at specific height.

3.2 Adiabatic LWC

To describe the change of LWC in a perfect adiabatic cloud the following equation is used (5) (Cermak and Bendix (2011); Toledo et al. (2021); Costabloz et al. (2024)).

$$\frac{d\mathrm{LWC}(z)}{dz} = \Gamma_{ad}(T(z), p(z)) \tag{5}$$

where z - height calculated from the base of the cloud. $\Gamma_{ad}(T(z), p(z))$ is the negative of the change in saturation mixing ratio with height for an ideal adiabatic cloud, in other words it is adiabatic condensation rate. The processes in stratus clouds are nearly adiabatic, the deviation from adiabatic conditions is introduced into equation as a parameter α. The fog is similar to stratus cloud, however to integrate Equation 5 apart from adding α a non-zero surface liquid water content ($\mathrm{LWC_0}$) must be taken into account.

$$\mathrm{LWC}(z) = \int_{z'=0}^{z'=z} \alpha(z')\Gamma_{ad}(T(z'), p(z'))\, dz' + \mathrm{LWC_0} \approx \Gamma_{ad}(T_B, p_B) \int_{z'=0}^{z'=z} \alpha(z')\, dz' + \mathrm{LWC_0} \tag{6}$$

LWP is defined as:

$$LWP = \int_{z'=0}^{z'=CTH} LWC(z')\, dz' \tag{7}$$

https://doi.org/10.5194/egusphere-2024-4074
Preprint. Discussion started: 17 February 2025

as fog base is at ground the integration take place from z' equal zero to cloud / fog top height (CTH).

In the case of shallow clouds $\Gamma_{ad}(T(z),p(z))$ can be assumed constant with height Brenguier (1991) $\Gamma_{ad}(T_B,p_B) = const.$ where T_B and p_B are respectively temperature and pressure at fog base / ground. Since the dependence of $\alpha(z)$ is unknown, the concept of equivalent adiabaticity $\alpha_{eq} = const.$ is introduced. The α_{eq} is defined as the constant adiabaticity value that would give the same LWP value when replacing $\alpha(z')$ in Eq. 6 and calculating LWP from Eq. (7). After taking $\alpha_{eq} = const.$ the formula for LWP becomes:

$$LWP = \frac{1}{2}\alpha_{eq}\Gamma_{ad}(T_B,p_B)\cdot CTH^2 + \mathrm{LWC}_0 \cdot CTH \tag{8}$$

The formula for LWC with the above assumptions is:

$$\mathrm{LWC}(z) = \alpha_{eq}\Gamma_{ad}(T_B,p_B)\cdot z + \mathrm{LWC}_0 \tag{9}$$

The method of calculating $\Gamma_{ad}(T_B,p_B)$ was taken the same as in Appendix A of the article Toledo et al. (2021).

To calculate what α_{eq} is, just reverse the Equation 8

$$\alpha_{eq} = \frac{2(\mathrm{LWP} - \mathrm{LWC}_0 \cdot CTH)}{\Gamma_{ad}(T_B,p_B)\cdot CTH^2} \tag{10}$$

In the literature, instead of α_{eq}, the parameter β is sometimes used, introduced by Betts (1982) as the in-cloud mixing parameter. This parameter measures departure from the adiabatic situation. The relation between α_{eq} and β is $\alpha_{eq} = 1 - \beta$.

In order to determine the existence of ground fog from satellite data, Cermak and Bendix (2011) proposed the LWC model for fog and stratus clouds. It is based on comparing the LWP obtained from the theoretical LWC profile with the height Eq. (8), with satellite data on LWP, CTH and T(CTH). In this way, it is possible to calculate the height of the cloud base. Toledo et al. (2021) based on Eq. (8) developed a one-column conceptual model of adiabatic continental fog to improve nowcasting of fog dissipation.

In later part of this article will be used:

- Γ_{ad} - adiabatic condensation rate of LWC,
- α_{eq} - deviation from Γ_{ad} which would give the same LWP for the whole cloud/fog,
- α_{fit} - deviation from Γ_{ad} obtained by fitting line to LWC dependence from height.
- Γ_{wa} - moist adiabatic lapse rate for T,
- γ_{fit} - deviation from Γ_{wa} obtained by fitting line to T dependence from height.

The Fig. 4 presents the visualization of listed above concepts.

3.3 1D Simulations radiation fluxes

Simulations were done in 1D using the Fu-Liou code Fu and Liou (1992, 1993).The Fu-Liou radiative transfer model is a sophisticated tool designed to accurately simulate radiative transfer in the Earth's atmosphere. Fu-Liou code uses δ- two/four

https://doi.org/10.5194/egusphere-2024-4074
Preprint. Discussion started: 17 February 2025

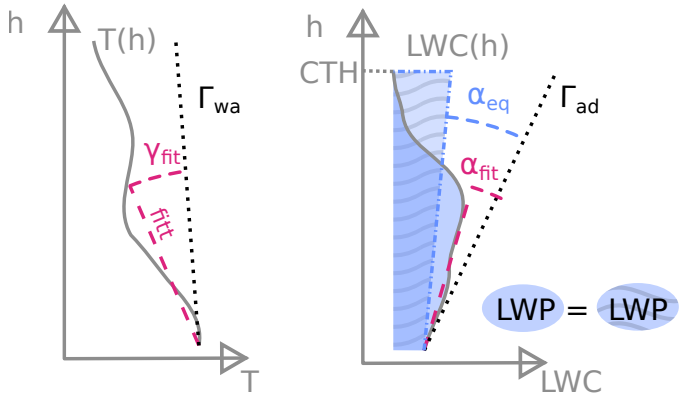

Figure 4. Representation of profile of T and LWC with added lines of Γ_{wa} and Γ_{ad} respectively. The γ_{fit} and α_{fit} represents the angle between best line fit to T and LWC respectively (from bottom to height of max LWC) and Γ_{wa} and Γ_{ad}. $\alpha_{eq} = const.$ is defined as deviation from Γ_{ad} which would give the same LWP as original data.

-flux approximation, which allows it to efficiently handle the complexities of radiation scattering and absorption by gases, aerosols, and cloud particles. Model covers six short waves (SW, $\lambda < 4$ μm) and 12 long waves (LW, Applied spectral bands $\lambda >= 4$ μm) making it well-suited for various atmospheric conditions. Fu-Liou model provide detailed insights into the interactions between cloud microphysics and radiation. The model vertical levels span from ground up to 10 km, with a greater density closer to the surface. In the first 100 m the grid was spaced every 10 m and from 100 m till 1 km every 100 m. Input to Fu-Liou model includes profiles of thermodynamic parameters, fog optical and microphysical quantities, aerosol optical properties, and surface reflectance and emissivity.

To perform simulations the following specific data were provided to the model:

- T and specific humidity profile. Data from soundings were combined with sounding from Tarnów (WMO station 12575) - more information is in Apendix A.
- r_{eff}; due to limitation of radiative transfer model; r_{eff} was set constant with height within the fog - the data from OPC-N3 were used to calculate the r_{eff}. OPC-N3 calculate the droplets counts in 24 bins. To calculate r_{eff} the bins from 7 till 24 were used - which corresponds to 1.15 to 20 μm - to remove aerosol particles.
- fog height - in the model was assumed that the fog starts at the surface and reach the CTH level. The top of the fog was determined as the point where LWC < 0.12 g·m^{-3}.
- aerosol optical depth (AOD) - measurements from CIMEL at SolarAOT^{upper} were taken. To adjust how much the beam is weakened by the vertical distance between upper and lower site; to the value of AOD was added the extinction coefficient (obtained from Aurora 4000 and AE-31) times the height difference (185 m) between both stations.

https://doi.org/10.5194/egusphere-2024-4074
Preprint. Discussion started: 17 February 2025

- aerosol single scattering albedo (SSA) - Based on AE-31 and Aurora 4000 located at SolarAOT^{upper} the SSA was calculated. The value of SSA at the moment of balloon sounding was obtained by linear interpolation.
- aerosol Angstrom exponent (AE) 440/870 nm. The values were rounded for the simulations to have similar conditions for each simulation, for 8-10 Sep. we assumed AE = 0.5 and for 11 Sep. AE = 1.0.

4 Case study: Valley of Strzyżów city

Fog was observed during three successive nights between 8 and 11 September 2023 in the valley of Strzyżów city. The balloon was launched after a fog was visible at the lower station. Apart from apparatus mounted on the balloon, there was at the ground Shadowgraph which was monitoring the LWC, r_{eff} and N_c (Fig. 5). The photo from the SolarAOT^{upper} station showing the top of the fog at 4:00 UTC is shown on Fig A2. During the experiment, the fog was not detected at the upper site. The Table 1 presents the duration of each fog and its division into stages. In this section will be described the evolution of each fog as well as its general pattern.

4.1 Meteorological overview

The area of Poland, as well as almost all of Europe, was under the influence of anticyclonic circulation of high pressure from Russia. The pressure on September 9 was constant and it was 1019 hPa, from 9 UTC on September 10 it began to slowly drop to reach the value of 1012 hPa on September 11 at 11 UTC. During days 8-10 September 2023 there was an event of Saharan dust over Poland. The AE measured for those days by CIMEL at SolarAOT^{upper} station where oscillating around 0.5 (for period of Saharan dust) and 1.0 (for morning of 11 September). The mean AOD during dust episode was not very high (0.19 at 500 nm). The sky was mostly cloudless A1, on September 9 in the morning cirrus clouds were visible, the average wind speed did not exceed 2.5 m·s^{-1}. Slow advection of hot air of tropical origin caused an inflow of Saharan mineral dust visible at 2-4 km a.g.l. on lidar data A1. The Fig.5d show aerosol scattering coefficient of light at 525 nm (ASC_{525}), for three nights of observations. On the night between 8-9 September 2023 ASC_{525} was below 100 Mm^{-1} which suggests moderate air quality conditions, just before the onset of fog 21:30-22:30 the values peak to 240 Mm^{-1} and after the end of fog values once again peak exceed very high level of 500 Mm^{-1}. These two peaks are probably due to industrial activity during inversion conditions and some turning on the heating systems in houses. The morning peak is coincident with inversion disappearance and the transport of pollution from the bottom of Strzyżów volley. On the night between 9 and 10 September the ASC_{525} was descending during the night from 150 to 100 Mm^{-1}, with a peak to 250 Mm^{-1} at 21 UTC. The cleanest conditions, with no evening peak of ASC_{525} were on night 10-11 September with values below 100 Mm^{-1}. At the upper station always in the evening and at night the values of ASC_{525} were below 100 Mm^{-1}. The air in the valley was trapped under the inversion of temperature. The inversion was starting at 18 at the night 08-09 and 09-10, and around 19 at night 10-11 Sep. 2023. The course of T at the valley each day was similar during the day, reaching a maximum of 24-26 °C, and reaching a minimum 12.5-13.5°C around 5 UTC 5. The inversion was disappearing around 8:40, 7:40, 8:10 respectively for days 9, 10, 11 Sep. 2023. The RH at SolarAOT lower station during fog was reaching 100%. The air at SolarAOT upper station was lower (RH=60-90%).

https://doi.org/10.5194/egusphere-2024-4074
Preprint. Discussion started: 17 February 2025

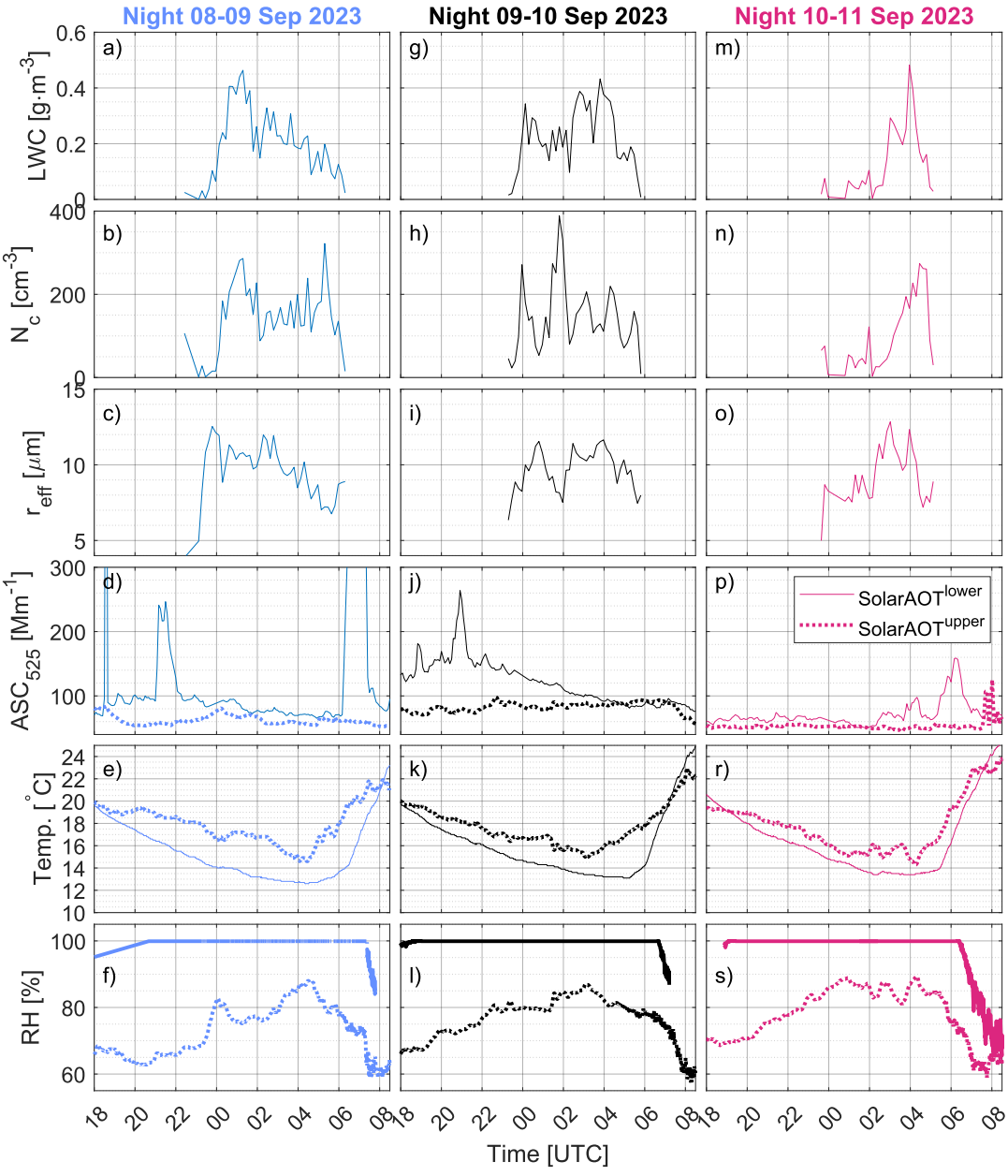

Figure 5. Temporal variability of weather condition on the ground for 09/10/11 September 2023 at the SolarAOT lower site (solid lines) and SolarAOT upper station (dotted line). On the panels **a),f),k)** is presented by solid line LWC form ShadowGraph, for reference when the soundings of the balloon with installed OPC-N3 occurred an overlay of Fig, 6 was added. Panels **b), g), l)** presents the N_c of droplets registered by ShadowGraph. Panels **c), h),** and **m)** shows r_{eff} obtained from ShadowGraph. Figure **d), i)** and **n)** presents the ASC at 525 nm from Aurora 4000; panels **e), j), o)** T from MetPak and panels **f), l), s)** RH.

https://doi.org/10.5194/egusphere-2024-4074
Preprint. Discussion started: 17 February 2025

4.2 Fog microphysics

Observed fogs were occurring mostly in moderate aerosol conditions, fog layer were located in the range of T inversion. The fog top was varying from sounding to sounding, mostly it was 85 m (max. 115 m) see Fig A2. The Fig. 7,Fig. 8 and Fig. 9 presents the T and RH with height as well as LWC, N_c and r_{eff} for each event of fog. The soundings starts at around 2 m above ground. It is worth to mention that at that stage of the year the sunrise is at 4:00 UTC (local time 6:00). Time is given in UTC, for this period of year UTC is -2 hours from local time.

4.2.1 Thin-to-tick transition

In the case of observed fogs the possible to check criteria of thin-to-thick transition were: temperature, CTH, and LWP. For Night 08-09 the criteria of LWP>15 g·m^{-2} has been fulfilled at 1:30, the criteria CTH>110 m at 4:09 (only for one profile). For Night 09-10 the criteria of LWP>15 g·m^{-2} has been fulfilled from the beginning of successful measurements (2:30), the criteria CTH>110 m at 5:15 (only for one profile). For Night 10-11 the criteria of LWP>15 g·m^{-2} has been at 3:10, the criteria CTH>110 m was not met.

In none of fog occurrence LWP exceeded 30 g·m^{-2} as proposed by Wærsted et al. (2017). In our opinion as most of the criteria were not fulfilled, we think the proposed adjustment of LWP criteria by Costabloz et al. (2024) is too week in our case. In our understanding none of the cases transitioned to thick fog.

4.2.2 Night 08-09 Sep. 2023

The fog on Night 08-09 Sep. 2023 was captured from the development state (23:00 - 1:41 UTC), through grown state (2:45 - 6:42 UTC) till disappearing (6:45-7:00 UTC). Fig. 7 presents the profiles of microphysics parameters such as LWC, N_c and r_{eff}, as well as atmospheric T and RH (the division for each stage is plotted in the Appendix Fig. A3a, Fig. A3b, Fig. A3c).

Costabloz et al. (2024) compares the registered profiles of LWC with the proposed theoretical profiles of LWC by Toledo et al. (2021). The proposed conceptual model of fog was introduced in Sec. 3.2, the equivalent adiabaticity α_{eq} is added on the figures presenting LWC.

In obtained profiles it is visible strong influence of ground to the profiles of LWC, T near the ground. Therefore, apart from α_{eq} to LWC a straight line was fitted from the 2 m to height of maximum LWC. In this way, the adiabatic profile scaling factor LWC was obtained α_{fit}, similarly as in the article Costabloz et al. (2024). According to the assumption by Cermak and Bendix (2011), above 80% of the height, the fog layer mixes with the dry air above it, which contributes to the reduction of LWC.

Based on measurements with OPC-N3 it was possible to compute LWC and LWP which are presented on Fig. 6. At 3 m above ground was mounted Shadowgraph which was constantly monitoring LWC during each episode (see Fig. 5).

Each of fog stages is described below.

- **Development of fog:** There were done 5 soundings between 23:00-2:34 see Fig. A3a. The T was decreasing with height from ground to 40 m a.g.l. Starting from T=12.0°C and decreasing at the rate $\gamma_{fit} \cdot \Gamma_{wa} = 0.48 \cdot (-5.0)$°C·km^{-1}. Above 40 m was the inversion with T reaching 14.7°C at 100 m. The top of fog was 65 m. The RH was constant equal

https://doi.org/10.5194/egusphere-2024-4074
Preprint. Discussion started: 17 February 2025

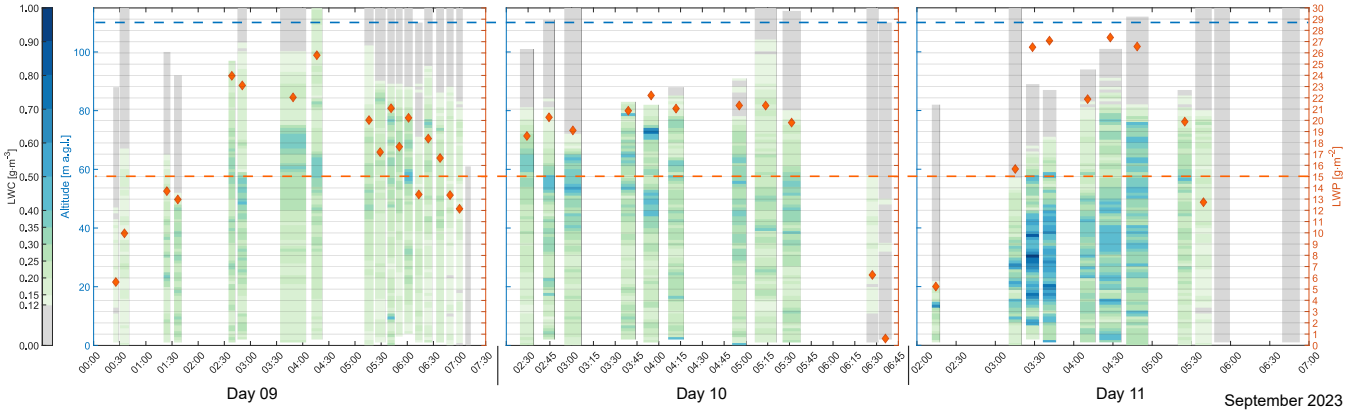

Figure 6. On the left axis changes of fog LWC with height for **a)** 09, **b)** 10, **c)** 11 September 2023. On the right axis is total fog LWP for each balloon sounding. Blue dashed line indicates the 110 m, orange line indicates LWP equal to 15 g·m^{-2}. Those are criteria indicating the transition of fog from thin to thick by Costabloz et al. (2024)

.

100% till 87 m and in the last 10 m drooping with height (96% at 100 m). LWC was slightly growing with height ($\alpha_{fit} \cdot \Gamma_{ad} = 1.34 \cdot 2.32$ g·m^{-3}·km^{-1}) from 0.18 to maximum 0.30 g·m^{-3} at 23 m a.g.l., till 36 m a.g.l. LWC was oscillating near value 0.26 g·m^{-3}, an above decreasing to CTH. The α_{eq} was 0.29. The LWC$_{\text{ShadowGraph}}$ (referring to LWC measured by ShadowGraph mounted 3 m a.g.l.) (Fig. 5) show that in the developing stage LWC$_{\text{ShadowGraph}}$ was fast increasing to reach it maximum 0.46 g·m^{-3} at 1:47. Values of LWC from ShadowGraph are higher than from OPC-N3. The LWP (Fig. 6) grow from 5.63 g·m^{-2} at 00:25 to 12.97 g·m^{-2} at 1:36. Mean N$_c$ was growing with height to 247 cm^{-3} at a 35 m. Than decreasing with height to 48 cm^{-3} at 65 m. The r$_{\text{eff}}$ was constantly decreasing with height from 11.2 to 5.7 μm at CTH.

– **Mature state of fog:** There were done 13 soundings from 2:34 till 6:42 (Fig. A3b). The T and RH have similar pattern with height as in previous stage. The fog deepen, it top was at 102 m. However the inversion of temperature starts higher, around 60 m above the ground, and the lower part lapse rate is higher $\gamma_{fit} \cdot \Gamma_{wa} = 1.16 \cdot (-5.1)$°C·km^{-1} The N$_c$ maximum equal to 410 cm^{-3} was at 48 m, above the N$_c$ decreases up to 65 cm^{-3} at 90 m. Above that the number of drops was constant. The r$_{\text{eff}}$ profile has changed, it can be divided into two areas. From the ground to a height of 88 m r$_{\text{eff}}$ it is almost constant (at bottom 9.2 μm; 8.3 μm at 88 m). From 88 m to CTH the r$_{\text{eff}}$ decreased with height sharply (mean at the top 5.2 μm). Because the N$_c$ maximum shifted upper also LWC maximum is at a higher altitude (56 m). The α_{fit} is positive, equal to 0.90 and α_{eq} equal to 0.30. The picture from the ShadowGraph shows that LWC$_{\text{ShadowGraph}}$ near the ground was decreasing in time from 2:57 and this fact was associated with decrease in r$_{\text{eff}}$ and not N$_c$.

– **Disappearing phase:** There were conducted 2 soundings in between 6:45 and 7:00 (Fig. A3c). The T is growing from ground to 27 m, above T is decreasing with height. Unfortunately the sounding with Vaisala radiosonde RS41

https://doi.org/10.5194/egusphere-2024-4074
Preprint. Discussion started: 17 February 2025

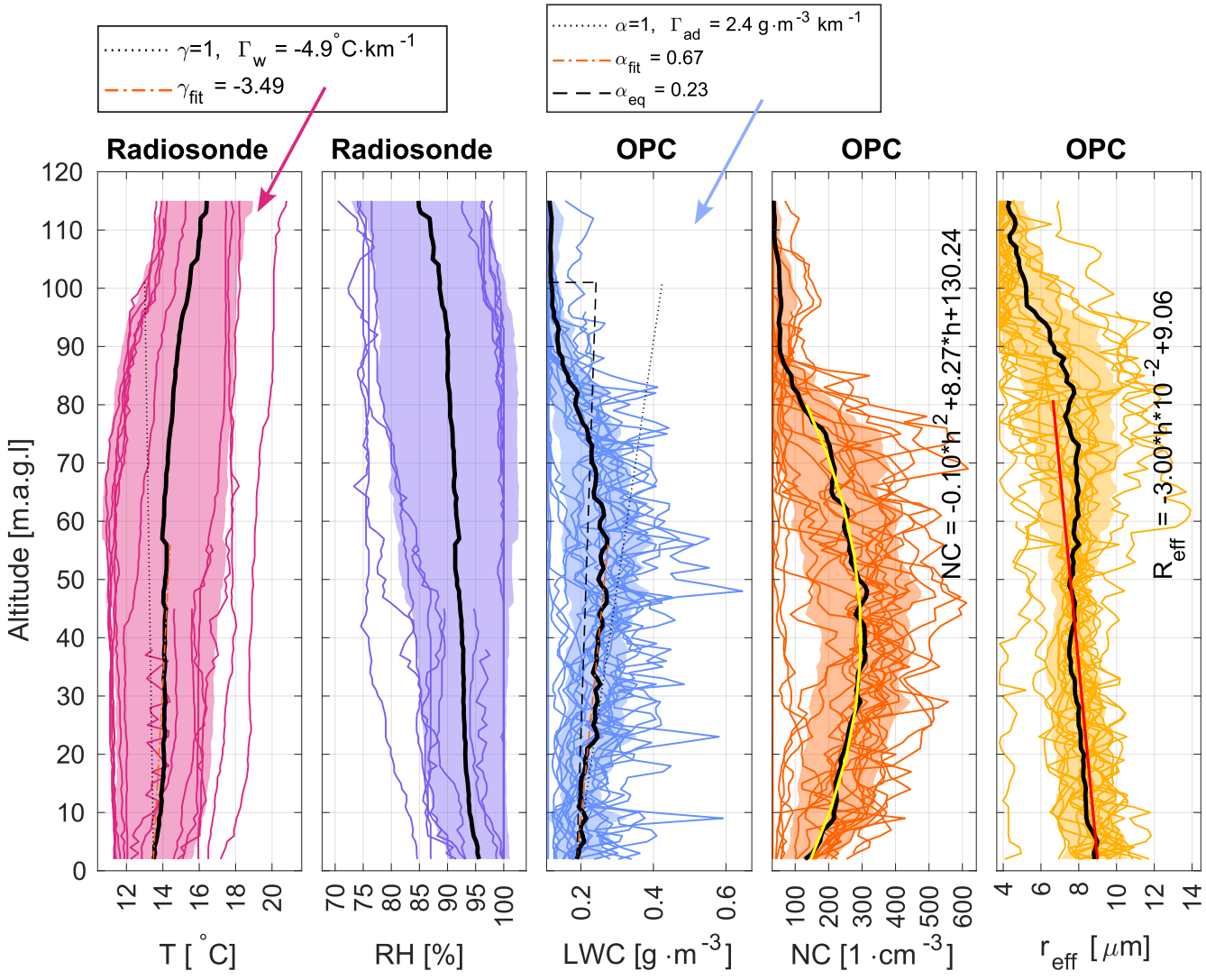

Figure 7. Vertical profiles of specific quantities measured by the balloon for night night 08-09 September 2023. From left: T and RH from Vaisala radiosonde RS41, LWC, N_c, r_{eff} within the fog from OPC-N3. Each colored line represents one balloon profile. Black thick line represents the mean of all the soundings, colored area represents range in between +/- standard deviation from the mean. On the r_{eff} plot the red line indicates the linear fit to the data. On the N_c plot the yellow line indicates the quadratic fit to the data. At the T plot dotted line presents the adiabatic lapse rate, dashed red line presents the linear fit to T from 3 m to height of maximum mean LWC. At the LWC plot dotted line presents the LWC adiabatic lapse rate, dashed red line presents the linear fit to LWC from 3 m to height of maximum mean LWC.

was interrupted at 45 m. Between two soundings spaced apart by less than 15 minutes the T profile shifted by +2°C. In this time the RH profile drooped by 5%. In the first 20 m the mean RH drooped from 96% near ground to 91% at 20 m. Fog evaporated quickly. The α_{eq} was positive, equal to 0.33. LWC was rising with height ($\alpha_{fit} \cdot \Gamma_{ad} = 0.42 \cdot$

https://doi.org/10.5194/egusphere-2024-4074
Preprint. Discussion started: 17 February 2025

2.39 g·m^{-3}·km^{-1}) reaching maximum at 72 m (mean LWC 0.26 g·m^{-3}) also at almost the same height the N_c has its maximum (488 cm^{-3} at 74 m). The layer above is characterize by rapid droop of both values to CTH. The r_{eff} was constant with height to 80 m, around 6.8 μm, apart from layer from ground to 18 m where r_{eff} was grater up to 9.5 μm.

The Fig. 7 shows the mean values with height for the whole night fog event from 08-09 Sep. 2023. For the whole fog event α_{eq} is 0.23. The first approximation of fog r_{eff} is a linear decrease with height while N_c can be fitted with quadratic equation.

$$N_c = -0.10 \cdot h^2 \cdot 10 + 8.27 \cdot h + 130.24 \ [\text{cm}^{-3}] \tag{11}$$

$$r_{eff} = 3.00 \cdot h \cdot 10^{-2} + 9.06 \ [\mu\text{m}]. \tag{12}$$

4.2.3 Night 09-10 Sep. 2023

Below are described the phases of fog from 09-10 Sep.2023:

- **Development of fog:** Due to malfunctioning of the apparatus the development of fog stage with microphysics measurements in vertical were not captured. The fog started at 00:00, however it not possible to determine when this stage ended. The first OPC-N3 registered sounding was at 2:34, with LWP> 15 g·m^{-2}. Based on measurements with Shadowgraph the LWC, N_c, grow constantly to 00:37 reaching local maximum of $LWC_{ShadowGraph}$ 0.34 g·m^{-3} and N_c 271 cm^{-3}. The r_{eff} reached its local maximum later at 1:17 equal to 11.6 μm. After the peak, values of LWC, N_c, r_{eff} were fluctuating reaching its global maxima N_c 388·cm^{-3} at 2:18 and minima r_{eff} 7.5μm at 2:28. There were done two profiles of T and RH, shown on Fig. A4a. Profile reaching higher altitude was done earlier at 00:53 and other was done after one hour. Profile of T was almost constant in first 40 m (12.65 at the ground), above was inversion of T which with time weakened. The RH was 100% till 67 m, above decreasing with height. However, one hour later the RH was constant 100% in the whole column from ground to 86 m.

- **Mature state of fog:** There were done 13 soundings from 2:45 till 6:42 (Fig. A4b). The fog height was 87 m. The T was decreasing with height till 50 m a.g.l., above was inversion of T. From ground till the CTH the RH was above 99.5%. Maximum LWC was at 53 m, LWC = 0.40 g·m^{-3}. To LWC from 2 m to 53 m was fitted line with growing rate equal to 0.51 of LWC adiabatic lapse rate. There max N_c was lower then in previous night 345 ·cm^{-3}. The r_{eff} at the ground was higher than in previous day fog, however the r_{eff} was decaying with height in first 30 m, from 30 to 63 m was constant approx. 9.0 μm and later decaying with height to CTH. The LWP (Fig. 6) was oscillating between 18-23 g·m^{-2}. Most of water was located in upper part of the fog between 30 and 70 m.

- **Disappearing phase:** There were conducted 5 soundings in between 6:30 and 7:30 UTC (Fig. A4c). The T at the 2 m a.g.l. and in the whole column was fast rising (from 11.9°C at 6:30 to 16.22°C at 7:30. The T in first 54 m was decaying with height, and higher there was an inversion of T. As the sun rose, the RH value decreased from 100% to 88% at 2 m above the ground. The parameters α_{fit} was 0.30 and α_{eq} was 0.24. The values of LWC were below 0.12

https://doi.org/10.5194/egusphere-2024-4074
Preprint. Discussion started: 17 February 2025

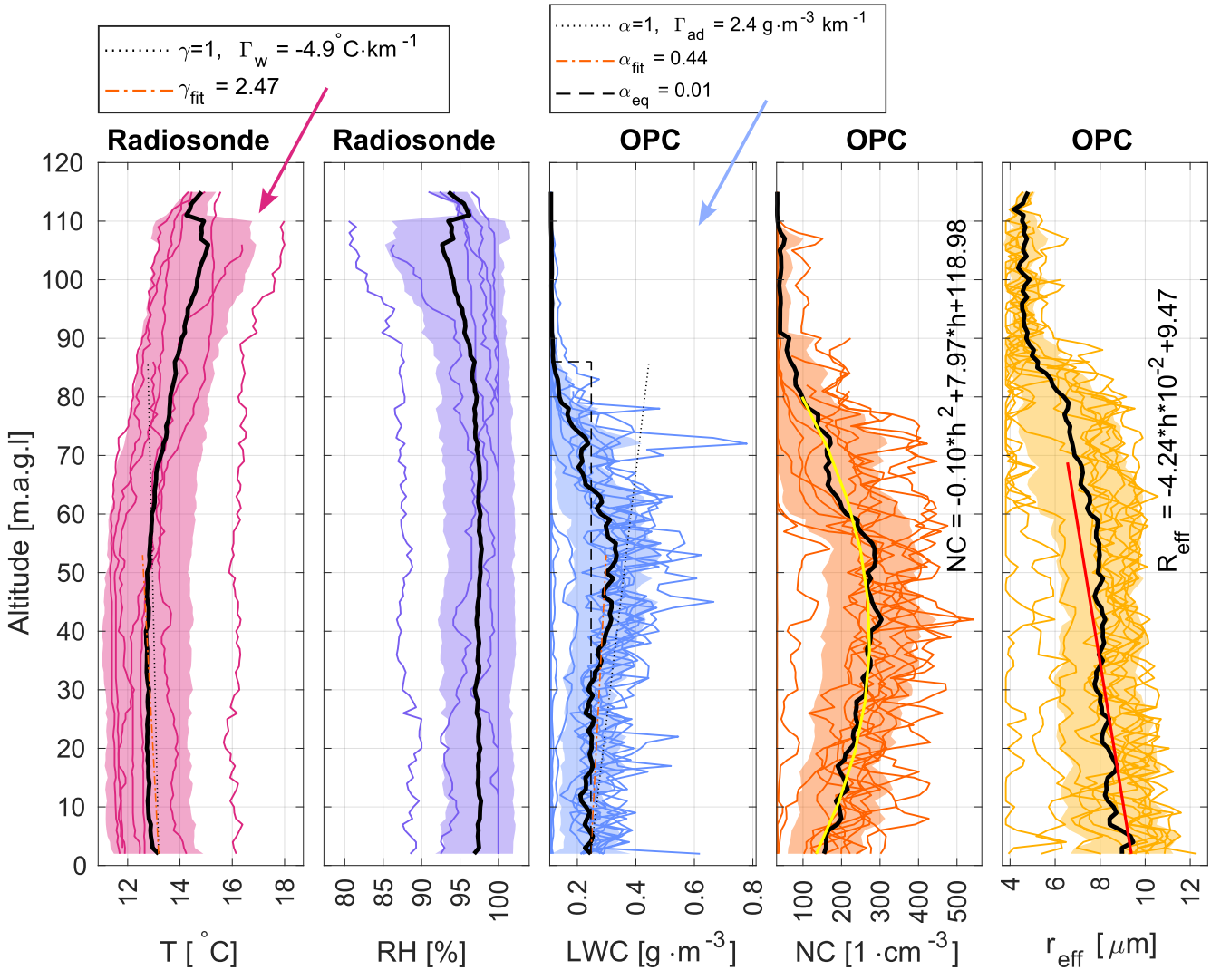

Figure 8. Vertical profiles of specific quantities measured by the balloon for night night 09-10 September 2023. The detailed description is given in caption 7.

in first 21 m above ground, maximum LWC = 0.15 was at 43 m. When fog almost disappear (6:23 UTC, Fig. 6) there where remaining fog patches at levels from 30-50 m, where LWC was above 0.15 g·m^{-3}. The fog peak fell to a height of 57 m. Fog droplet diameter was decaying with height from 6.7 μm at 4 m above ground to 4.8 μm at CTH. The N_c was oscillating around value 170 cm^{-3} between 24 m and 56 m. The fog was disappearing from both above and below.

The T in the first 53 m was almost constant with height. In this layer the LWC was increasing with height at rate $\alpha_{fit} \cdot \Gamma_{ad} = 0.44 \cdot 2.4$ g·m^{-3}·km^{-1}) reaching local maximum LWC=0.33 g·m^{-3} at 53 m. The value of α_{eq} was almost zero (0.01). Fig. 8

https://doi.org/10.5194/egusphere-2024-4074
Preprint. Discussion started: 17 February 2025

summaries the microphysical properties of fog event at 09-10 Sep. 2023. To values of N_c and r_{eff} were fitted following curves:

$$N_c = -0.10 \cdot h^2 \cdot 10 + 7.97 \cdot h + 118.98 \ [\mathrm{cm}^{-3}], \tag{13}$$

$$r_{eff} = 4.29 \cdot h \cdot 10^{-2} + 9.47 \ [\mu\mathrm{m}], \tag{14}$$

4.2.4 Night 10-11 Sep. 2023

The fog pattern on night 10-11 Sep. look different from previous nights. The fog could not form until 3:08, when it started to develop with an abrupt jump in LWC from 0.05 at 3:08 to 0.30 at 3:31 UTC, the maximum peak in LWC observed on the ground by ShadowGraph was at 4:27 UTC equal to 0.48 g·m^{-3}. With fast growth, reaching high LWC values (mean 0.48 g·m^{-3}) in the fog body from 10-50 m, with maximum LWC 0.97 g·m^{-3} at 31 m at 3:23 UTC. At 4:40 UTC the high values of LWC above 0.40 g·m^{-3} where distributed in the range from fog bottom to 80 m above. As it quickly appeared it also quickly diapered by 5:40 UTC. However as before, the fog was more vanishing from bottom than from the top.

During night 10-11 Sep. 2023 all phases of fog were captured, below each stage is described in detail. This event of fog developed later in the night that previous cases and it had more abrupt behavior.

- **Development of fog:** Between midnight and 2:28 the ShadowGraph was detecting droplets however the $LWC_{ShadowGraph}$ was below 0.1 g·m^{-3}. There were performed two soundings one with OPC-N3 and one with Vaisala radiosonde RS41 between 2:00 and 3:02 (Fig. A5a). The profile from 2:11 shows the fog was just forming. LWP was 5.23 g·m^{-2}. Fog was confined to first 23 m in height. Even though the fog was shallow it at some levels had high LWC values (max. LWC was 0.67 g·m^{-3} at 13 m). The $\alpha_{eq} = -3.22$, however α_{fit} was -0.15. The fog was dense - maximum N_c was 416 cm^{-3} at 18 m. The r_{eff} was decreasing with height (9.8 μm at 2 m and 6.0 μm at CTH). The profile from Vaisala radiosonde RS41 at 2:43 shows that the T was almost constant in first 40 m around 12.7-12.8°C, later slightly increasing with height to 14.2°C at 100 m. The profile of RH was constant with height, however the air was not fully saturated, RH was around 98.5%. ShadowGraph show that LWC drooped to 0 at 2:38 and in the next hour fast rebuild LWC to value 0.30 g·m^{-3}. This was correlated with fast growing of r_{eff} from 7.8 μm to 12.8 μm, as N_c was at low value 2-65 cm^{-3}.

- **Mature state of fog:** Between 3:10 and 5:30 was conducted 8 soundings with balloon (Fig. A5b). The fog deepen to 83 m. Profile of T and RH has changed. Only in the first 10 m the RH was above 99.5%. Above was decreasing with height to 85.5% at 60 m. Unfortunately the sounding with Vaisala radiosonde RS41 did not reach CTH. There was a strong inversion, fitted lapse rate was is$\gamma_{fit} \cdot \Gamma_{wa} = -11.82 \cdot -4.97$°C·km^{-1}. The T was increasing from 12.3°C at ground to 15.8°C at 60 m. The profile of N_c has different form than in previous fog events, it consists of two protrusions with a maximum at 25 m (377 cm^{-3}) and 70 m (257 cm^{-3}), and a decrease in the number of drops at a height of 50 m. The r_{eff} is slightly decreasing in the layer from ground (10.0 μm) to 60 m (8.8 μm). From 60 m to CTH the r_{eff} decreases with height more abrupt (5.5 μm at CTH). Profile of LWC shows more intermittent pattern with values highly fluctuating

https://doi.org/10.5194/egusphere-2024-4074
Preprint. Discussion started: 17 February 2025

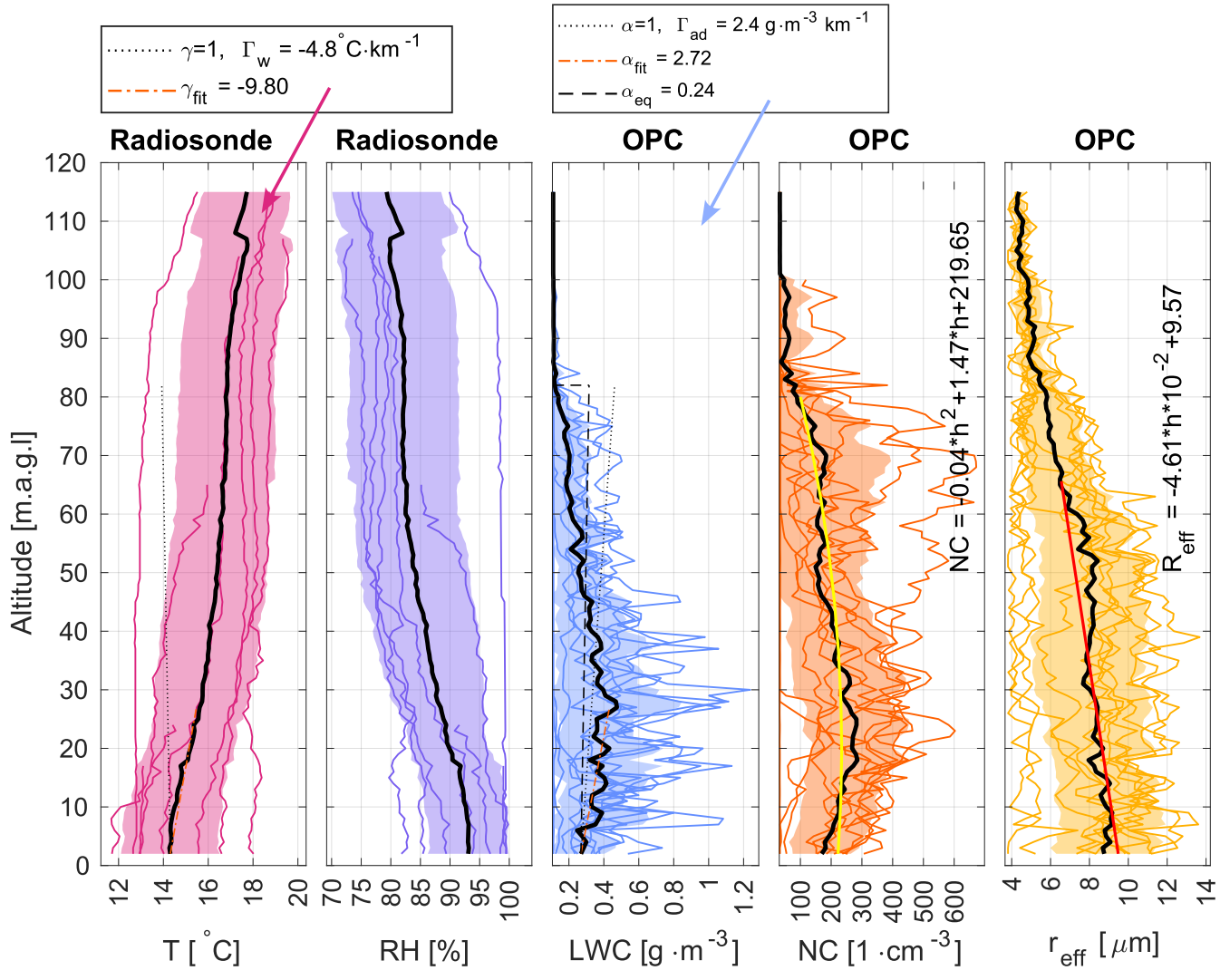

Figure 9. Vertical profiles of specific quantities measured by the balloon for night night 10-11 September 2023. The detailed description is given in caption 7.

from 0.2 to 1.2 g·m^{-3} having a peak at 27 m equal to 0.67 g·m^{-3}. The $\alpha_{eq} = 0.56$ and fitted $\alpha_{fit} = 4.80$. The LWP was the highest from all three events, for four soundings LWP was above 26.5 g·m^{-2} (maximum 27.36 g·m^{-2} at 4:27).

– **Disappearing phase:** The last phase of fog was observed from 5:30 to 6:00, there were done 2 soundings with OPC-N3, in the Fig. A5c are also included two soundings of T and RH between 6:00 and 6:33. The CTH was at 79 m. The LWC was growing with height, maximum LWC was almost at the CTH (max LWC = 0.19 g·m^{-3} at 75 m). Because of location of max. LWC near CTH the $\alpha_{eq} = 0.32$ was similar to $\alpha_{fit} = 0.30$. The N_c was increasing with height to 27 m where

https://doi.org/10.5194/egusphere-2024-4074
Preprint. Discussion started: 17 February 2025

it had maximum 190 cm^{-3}, and than oscillating around 145 cm^{-3} till 43 m above ground, and sharply decreasing to 62 cm^{-3} at 48 m. The r_{eff} was slightly decreasing with height, with fluctuations around 6 μm.

Fig. 9 summarize the microphysical properties of fog event at 10-11 Sep. 2023. The α_{eq} for the whole event was 0.24. To values of N_c and r_{eff} were fitted following curves:

$$N_c = -0.04 \cdot h^2 \cdot 10 + 1.47 \cdot h + 219.65 \ [\mathrm{cm}^{-3}], \tag{15}$$

$$r_{eff} = 4.61 \cdot h \cdot 10^{-2} + 9.57 \ [\mu\mathrm{m}]. \tag{16}$$

4.3 Evolution of fog droplet spectrum

The OPC-N3 measures droplets in 24 bins, therefore it was possible to compute vDSD(r) presented at Fig. 10 **a)**. The vDSD is presented from bins of radius from 1.15 to 20 μm to remove aerosol particles. As it was stated by Nurowska et al. (2023) even though manufacturer declare that the upper limit of the last bin is 20 μm, in fact the last bin also counts larger particles.

The obtained vDSD was not calibrated with ShadowGraph. Vertical profile of vDSD gives information which droplets give biggest contribution to LWC at specific height. Apart from vDSD at Fig. 10 on panel **b)** is shown vDSD with normalization. Normalization consists of dividing the whole spectrum at a given height by $\sum_{r_b} \mathrm{vDSD}(r_b)$ from a given height. In this way, Fig. 10 **b)** shows what percentage of the entire spectrum at a given height is contributed by the volume of drops from a given bin. Fig. 10 **a)** with vDSD presents on which height is produced most LWC and by which droplets, meanwhile Fig. 10 **b)** allows to analyze the spectrum in region where LWC is low (e.g. at top of fog layer, while vanishing). Apart from vDSD for the whole episode, in the Appendix are shown vDSD (Fig. A6) for each stage of fog: beginning, mature, disappearing. In this section is describe how LWC, LWP and droplet spectrum evolve during the occurrence of fog for each night case.

From vDSD (Fig. 10) it is visible that most of the LWC is associated with two drop radius regions. First region is described by asymmetric distribution. The maximum value of distribution is associated with radius 4-5 μm. The distribution has a bigger slope from left side (droplets smaller than maximum). Second region is a peak for droplets of radius bigger than 18.5 μm ($r_{>18.5}$). Big droplets are found in the whole range of altitudes, however there is more of them when closer to the ground. In 10 m region closest to the ground droplets with $r_{>18.5}$ are contributing to total LWC up to 40%. In this layer, also when closer to the ground, the smaller the contribution to LWC is made by droplets below 7 μm and larger by those above 7 μm. Above 40 m with increasing height, the 4-5 μm peak shifts towards larger droplets of the order of 8-9 μm.

Near the ground was located ShadowGraph, Figure 11 presents the comparison between the vDSD obtained from ShadowGraph and OPC-N3. ShadowGraph shows that near ground there are droplets of radius grater than 20 μm, and that in case of OPC-N3 those droplets are counted in the last bin. Although OPC-N3 is not calibrated to match the vDSD values it has similar pattern of the spectrum as ShadowGraph.

Subsequent fogs nights had increasingly larger LWC, this was related to the appearance of droplets in the size of 7-17 μm, and not to the increase in the number of droplets in the size of 4-5 μm. The fog on night 08-09 Sep. had maximum CTH at

https://doi.org/10.5194/egusphere-2024-4074
Preprint. Discussion started: 17 February 2025

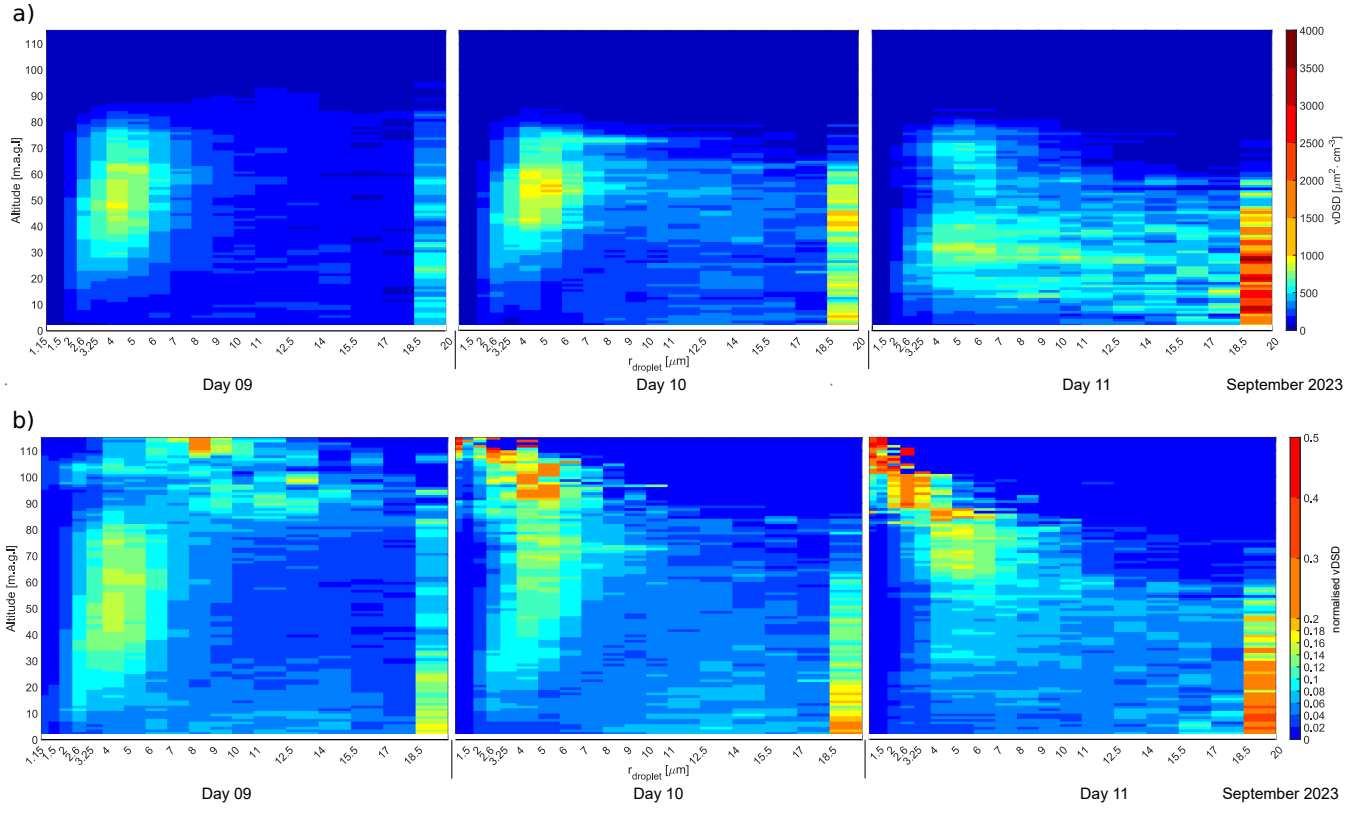

Figure 10. Vertical profile of vDSD and normalized vDSD for 8-11 September 2023 fog occurrence. Panel **a)** presents the vDSD. The scale is divided into steps of 100 $\mu m^2 \cdot cm^{-3}$ from 0 to 1000$\mu m^2 \cdot cm^{-3}$ and then in steps of 500 $\mu m^2 \cdot cm^{-3}$. Panel **b)** presents the normalized at each height vDSD. Figure presents what percentage of the entire spectrum at a given height is contributed by the volume of drops from a given bin.

102 m, the LWC above 80 m was below 0.2 $g \cdot m^{-3}$. To LWC mostly contributed droplets of radius 8-14 μm. Above CTH the most water is in the form of small droplets with has decreasing radius with increasing altitude.

In the Appendix the Fig. A6 presents vDSD for three stages of fog for each day. Even in the initial stage of the fog there were already large drops with $r_{>18.5}$, the fog started to grow in thickness from the bottom. In the case of the fog from the nights of 8-9 and 9-10 Sep., with increasing height, water was stored by drops with increasingly larger radii between 2-10 μm. In the case of the fog from the night of 10 to 11 Sep., with increasing height, an inverse relationship occurs - increasingly smaller drops store the most water from the range of radii 2.0-18.5 μm.

In the case of 08-09 and 10-11 Sep., the fog disappeared more from the bottom than from the top. For the case of 9-10 Sep., only small drops from the range of 2-7 μm at a height of 20-60 m contributed to the LWC. For all cases, large drops $r_{>18.5}$ stopped contributing significantly to the LWC when the fog was disappearing.

https://doi.org/10.5194/egusphere-2024-4074
Preprint. Discussion started: 17 February 2025

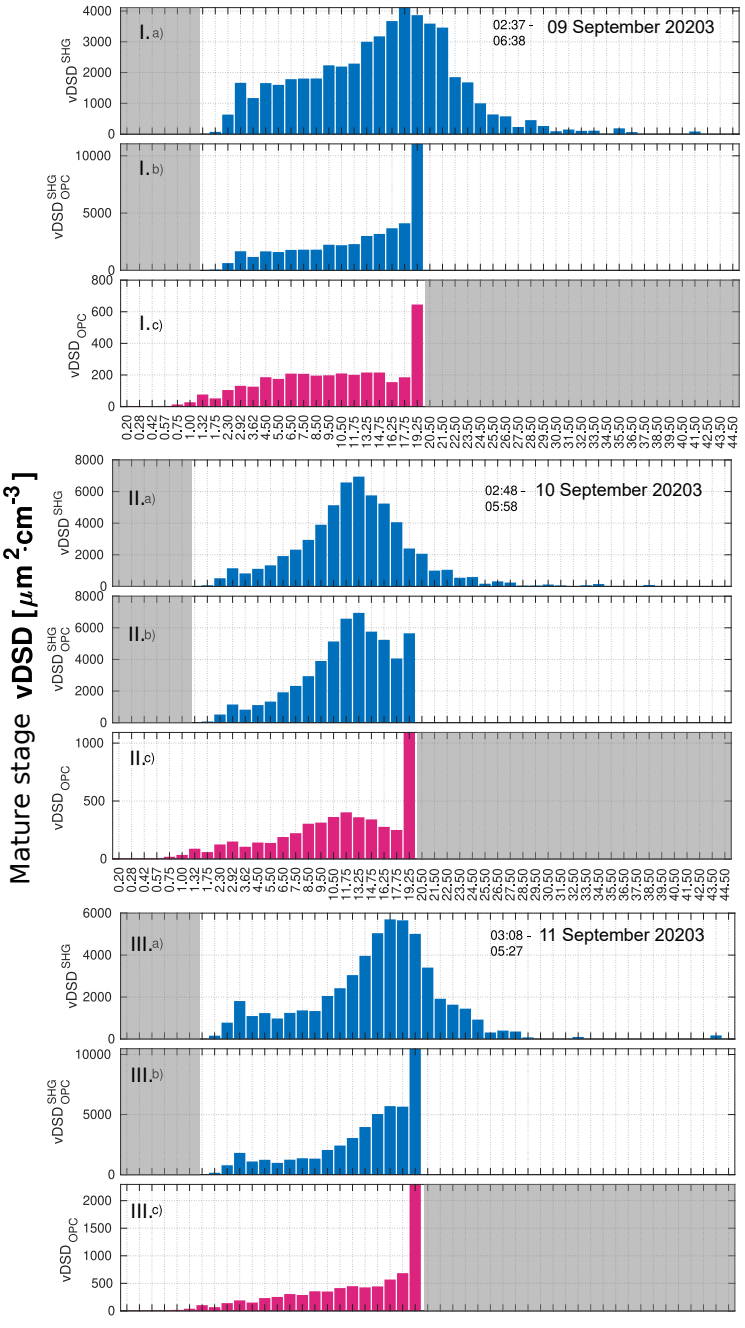

Figure 11. vDSD near ground for mature stage of night events of fog on: I. 08-09 Sep., II. 09 - 10 Sep., III. 10-11 Sep. 2023. Panels **a)** and **b)** presents the vDSD obtained from Shadowgraph, while **c)** presents vDSD from OPC-N3. The X axis is representing the radius bins same as in OPC-N3 plus additionally grater bins (above 20 μm) visible only by Shadowgraph. The panels **b)** presents the same vDSD as panel **a)** however all the droplets with radius grater than 20 μm are counted as part of the last bin of OPC-N3 (18.5-20 μm) - this is done to be able to compare the vDSD from OPC-N3 and Shadowgraph. The imaging area for a given device is marked in white.

https://doi.org/10.5194/egusphere-2024-4074
Preprint. Discussion started: 17 February 2025

4.4 Optical, microphysical and radiation closure

The optical, microphysical and radiation closure was done for the case study in the valley of Strzyżów city in September 2023. For performing the simulations only cases when setup 1 (with OPC-N3) was attached to the balloon and data were properly collected. In total there were 41 soundings.

On the Figure 13 and 14 by black line are presented the measured SW and LW radiation fluxes from SolarAOT^{upper} and SolarAOT$_{lower}$ station. By the yellow dashed line is presented the simulation result for clear-sky, while the orange circles present the result of simulation with implemented fog conditions, based on soundings. During 09 Sep. there were observed cirrus clouds therefore the SW radiation during the day at SolarAOT station has a rugged time course. During the day 10 Sep. the sky was clear but during dust long-range transport. To compare the clear-sky conditions between model and observation data from 10. Sep. was used. The comparison is show in the Fig. 12, as well as the comparison between fog modeled cases and observational data. Model was run with the use of meteorological soundings from Tarnów station - which are done only twice per day 00 and 12 UTC. Therefore for comparison of clear-sky conditions in model and observation only data from near the sounding at 12 UTC $\pm$ 2 hours were used. On the scatter plots are shown also linear fits to the data. The SW radiation for clear-sky conditions for both stations is almost 1:1 from the observation and model:

$$SW_{upper}^{obs} = 1.01 \cdot SW_{upper}^{mod} - 0.3 \tag{17}$$

$$SW_{lower}^{obs} = 1.01 \cdot SW_{lower}^{mod} - 11.7 \tag{18}$$

Similarly in the case of model with implemented fog (note that upper site was above the for layer):

$$SW_{upper}^{obs} = 1.00 \cdot SW_{upper}^{mod} - 6.1 \tag{19}$$

$$SW_{lower}^{obs} = 1.05 \cdot SW_{lower}^{mod} - 9.7 \tag{20}$$

The obtained linear fit is worse in the case of LW radiation for fog conditions. As fog is occurring mostly at night there is smaller variability of LW flux and mostly points are located in one area. One data point stands out from the rest, for 10-11 Sep., this is at the dissipation of fog, when the sounding did not show fog and the instruments showed the opposite.

$$LW_{upper}^{obs} = 0.53 \cdot LW_{upper}^{mod} + 164.5 \tag{21}$$

$$LW_{lower}^{obs} = 0.38 \cdot LW_{lower}^{mod} + 217.4 \tag{22}$$

The Table 2 presents the statistics between simulated and measured SW and LW flux for clear-sky (no fog) and fog conditions. For clear-sky SW the model flux at SolarAOT^{upper} station are underestimated, RMSE (root mean square error) for 9

https://doi.org/10.5194/egusphere-2024-4074
Preprint. Discussion started: 17 February 2025

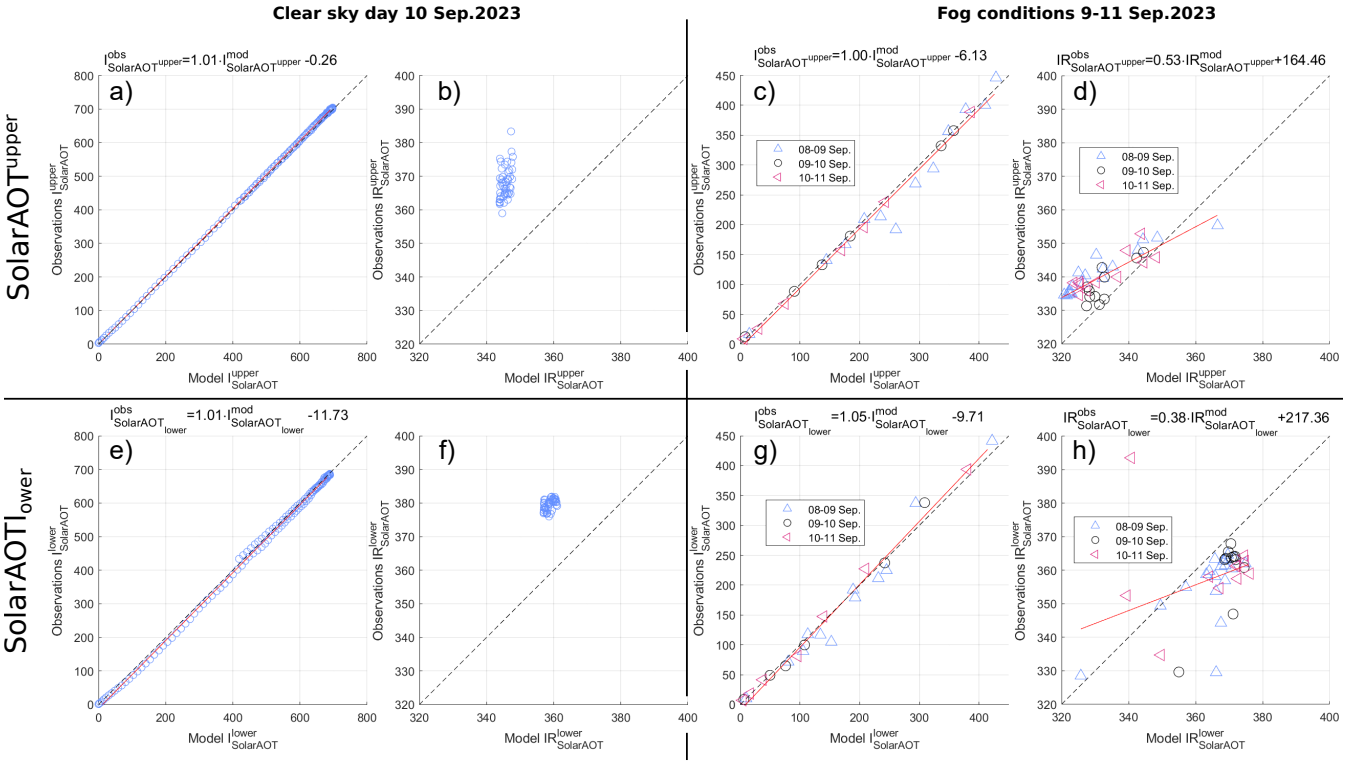

Figure 12. Comparison of observational data with model predictions of SW (Panel **a)**, **e)**, **c)**, **g)**) and LW (Panel **b)**, **d)**, **f)**, **h)**) fluxes for two locations: SolarAOT^{upper} (Panels **a-d)**) and SolarAOT$_{lower}$ station ((Panels **e-f)**)). Panels **a)**, **b)**, **e)**, **f)** presents the situation with clear-sky conditions which where on Sep. 10. Panels **c)**, **d)**, **g)**, **h)** presents the comparison of SW and LW radiation during fog conditions. Red solid line presents the linear fit to the data, blue triangles data from night between 8 and 9 September, black circles fog data from night between 9 and 10 September and pink triangles represents data taken during night from 10 to 11 September 2023. The equation for each fit is presented above corresponding panel.

and 10 Sep. is accordingly 25.5 and 5.4 W·m^{-2}. Relatively high RMSE during 9 Sep. is due to cirrus cloud contamination which was not considered in the radiative transfer model. For the SolarAOT^{lower} station, the RMSE is 22.9 and 10.4 W·m^{-2}, respectively, for 9 and 10 Sep. The model LW flux at both sites is underestimated and RMSE does not exceed 26 W·m^{-2}. The model shows slightly better agreement during fog conditions.

When the fog conditions where applied the results for SolarAOT^{upper} station where slightly overestimated (up 10 W·m^{-2}) for SW flux and underestimated (up to 10 W·m^{-2}) for LW flux. In the case of the SolarAOT^{lower} both SW and LW bias also do not exceed 10 W·m^{-2}. The RMSE exceeds 20 W·m^{-2} only during cirrus conditions (9 Sep.). A slightly higher RMSE (SW and LW range) was obtained for the lower than for the upper station. Generally, an agreement between SW and LW fluxes at both sites is really good. Even for fog conditions at the lower site the MBE is very low (up to 10 W·m^{-2}) and RMSE not exceed 20 W·m^{-2}.

https://doi.org/10.5194/egusphere-2024-4074
Preprint. Discussion started: 17 February 2025

The apparatus at SolarAOT upper and lower station measures the total net radiation (NET; downward by minus upward SW+LW fluxes), which is presented on the lowest panel of Fig. 13. During the first night of observations it is visible that between 00:00 and 00:40 the NET radiation at the SolarAOT lower station changed from -20 to -6 W·m^{-2}. After development of fog the NET radiation at lower station was around 0 W·m^{-2} it become positive after the sunrise. The difference between lower and upper NET radiation during night fog was around 60 W·m^{-2}. When the fog disappeared (7:00) there is a visible abrupt jump of 160 W·m^{-2} at the lower station within 15 minutes. For the night 9-10 Sept. 2023 the fog also started to develop around midnight (at 00:50 the NET radiation was -6 W·m^{-2}). The NET radiation at SolarAOT lower become positive after sunrise and a jump of 140 W·m^{-2} occurred at the moment of disappearing of fog at 6:20-6:35. During the last night of observations the NET radiation at lower station was still -30 W·m^{-2} at 02:00. From 02:00 the NET radiation was constantly increasing until the sunrise when reached 0 W·m^{-2}. The fog disappeared quickly, in less than ten minutes at 05:35 the NET radiation changed by 120 W·m^{-2}.

Having information on radiation fluxes at two levels allows to investigate the sensitivity of the change in LW radiation by the fog LWP. Fig. 15 shows the relationship between the modeled LWP content and the modeled difference in LW radiation between the upper and lower station. In addition to the modeled values, the lower panel of Fig. 15 shows the relationship for the data observed at both stations and the measured on the balloon LWP in the fog. In both graphs, the data are arranged according to a linear relationship (Pearson correlation coefficient for modeled data is -0.81 and for observation is -0.59), to the modeled data was fitted a straight line given by equation:

$$\Delta \mathrm{IR} = -1.47\ [\mathrm{W\ g^{-1}}] \cdot \mathrm{LWP} - 4.16\ [\mathrm{W\ m^{-2}}] \tag{23}$$

to the observed data was fitted a straight line:

$$\Delta \mathrm{IR} = -1.17\ [\mathrm{W\ g^{-1}}] \cdot \mathrm{LWP} - 5.87\ [\mathrm{W\ m^{-2}}]. \tag{24}$$

5 Conclusions

The purpose of this study was to capture vertical profiles of the microphysical and thermodynamic characteristics within fog layers, utilizing in situ data gathered by a tethered balloon during the field campaign. In this article are analyzed three cases of radiative fog which occurred in valley of Strzyżów city (Southeastern Poland) in September 2023. In total there were performed 74 soundings, of which 41 were done with OPC-N3 - which allows for droplet spectra calculations. The observed three cases had similar weather conditions (temperature - T, relative humidity - RH, ASC_{525}). For each case the liquid water path (LWP) exceeded 15 g·m^{-2}, none of the cases transitioned to thick fog.

In case of the quasi-adiabatic boundary clouds Brenguier et al. (2000) droplet number concentration (N_c) was constant with height and the increase of liquid water content (LWC) with height was associated with the increase droplet radii. In simulations of Atlantic stratocumulus used by Chang and Li (2002) also increase of LWC with height was associated with the increase

https://doi.org/10.5194/egusphere-2024-4074
Preprint. Discussion started: 17 February 2025

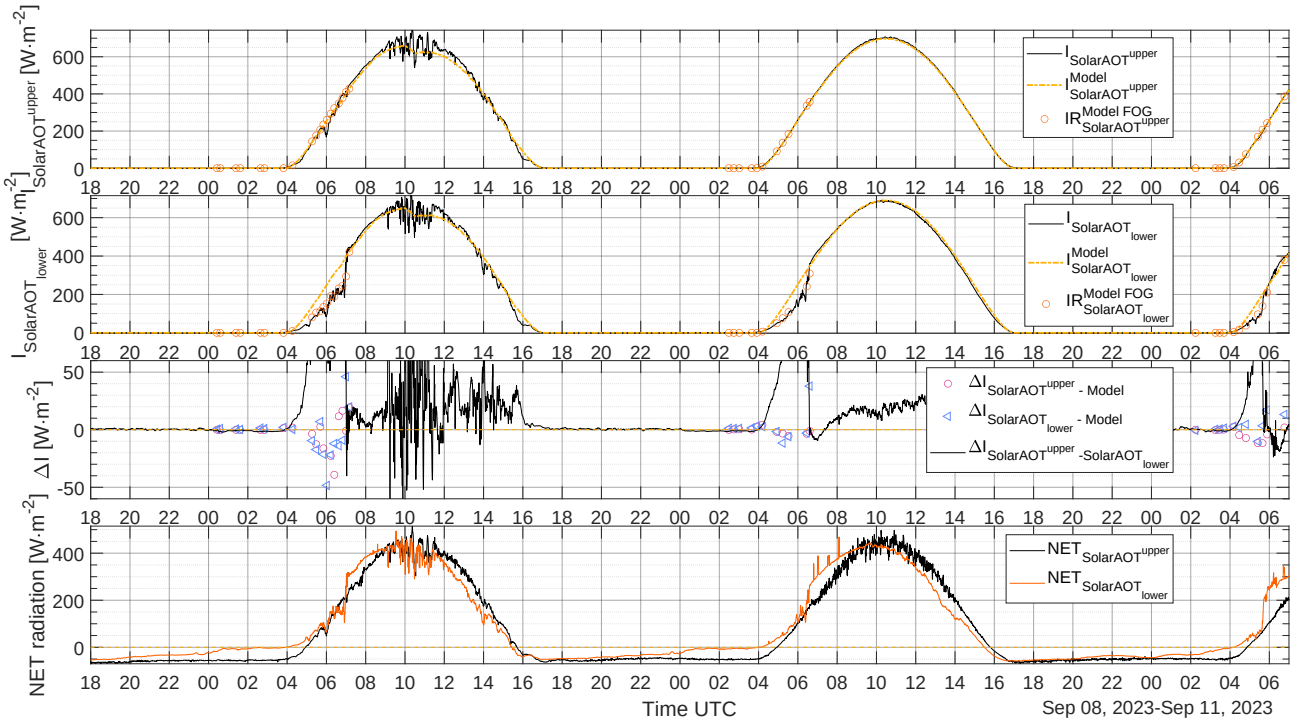

Figure 13. SW flux for SolarAOT upper and lower station. Black solid line measured data, yellow dashed line - model result for no fog conditions, orange circles - model results for fog conditions measured by soundings. Third panel from the top presents difference in SW flux between upper and lower site (solid line), pink circles represents difference between SolarAOT upper station and model when there were implemented fog conditions. Blue squares represent difference between SolarAOT lower station and model with implemented fog conditions. The lowest panel presents the total net radiation for SolarAOT upper (black line) and SolarAOT lower station (orange line).

https://doi.org/10.5194/egusphere-2024-4074
Preprint. Discussion started: 17 February 2025

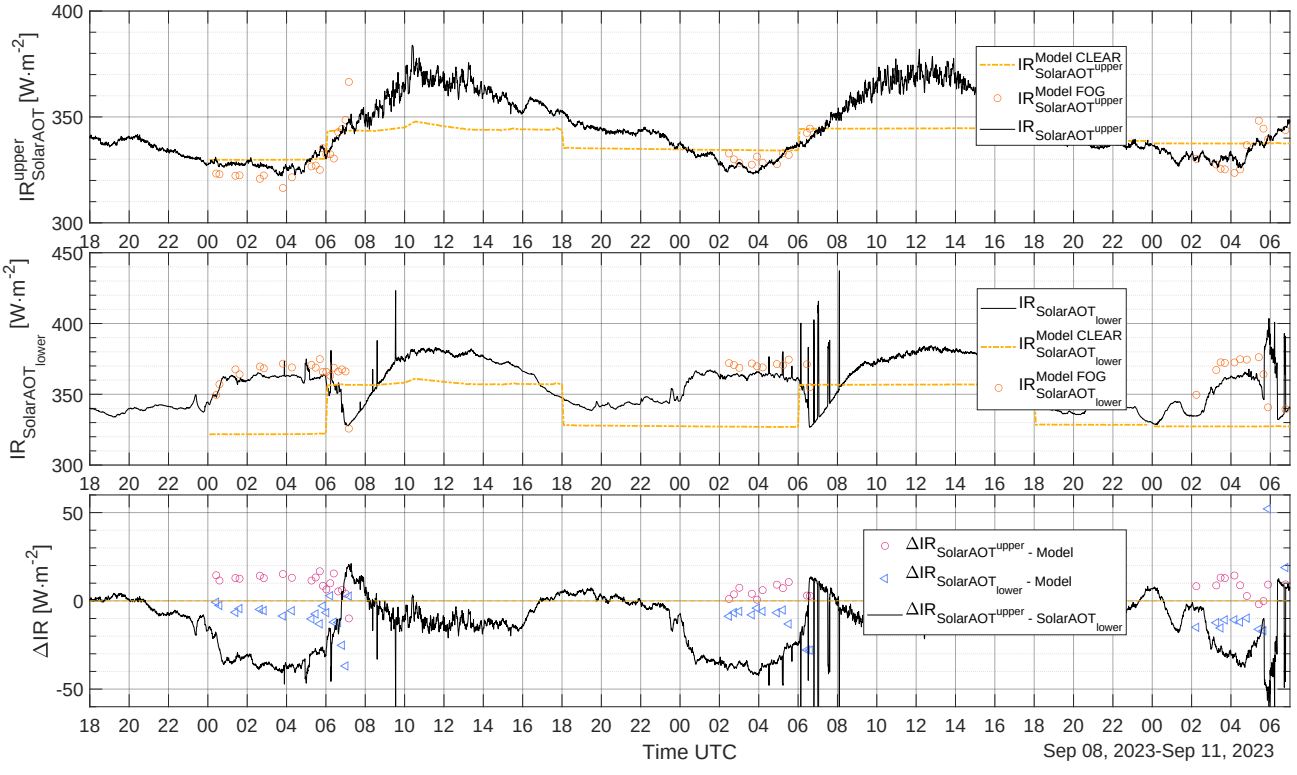

Figure 14. LW flux for **a)** upper and **b)** lower station. Black solid line measured data, yellow dashed line - model result for no fog conditions, orange circles - model results for fog conditions measured by soundings. Panel **c)** presents with solid line difference in LW flux between $SolarAOT^{upper}$ and $SolarAOT_{lower}$ station, pink circles represent difference between upper station and model with fog conditions implemented and blue squares represent difference between lower station and model with fog conditions.

https://doi.org/10.5194/egusphere-2024-4074
Preprint. Discussion started: 17 February 2025

MBE [W·m^{-2}]						
Day	09 Sep.		10 Sep.		11 Sep.	
Model run	every 5 min	when sounding	every 5 min	when sounding	every 5 min	when sounding
Fog implementation	**no**	**yes**	**no**	**yes**	**no**	**yes**
Time	7-17 UTC	4 -7 UTC	7-17 UTC	4 -7 UTC	7-17 UTC	4 -7 UTC
$I_{SolarAOT^{upper}}$	-12.6 ± 22.3	10.2 ± 23.8	-4.5 ± 2.9	1.7 ± 3.3	-	4.9 ± 5.8
$I_{SolarAOT^{lower}}$	-0.8 ± 23.0	6.1 ± 22.8	6.7 ± 8.1	-1.2 ± 14.6	-	-4.6 ± 10.4
$I_{SolarAOT^{lower}}$ (-cirrus bias)	11.8 ± 13.7	1.0 ± 23.3				
Time	10-14 UTC	0 -7 UTC	10-14 UTC	0 -7 UTC		0 -7 UTC
$IR_{SolarAOT^{upper}}$	-22.4 ± 4.4	-10.2 ± 6.4	-25.1 ± 4.2	-5.0 ± 3.4	-	-7.6 ± 5.4
$IR_{SolarAOT^{lower}}$	-20.7 ± 1.5	8.6 ± 8.8	-22.3 ± 3.1	10.2 ± 7.8	-	4.0 ± 20.5
RMSE [W·m^{-2}]						
Day	09 Sep.		10 Sep.		11 Sep.	
Model run	every 5 min	when sounding	every 5 min	when sounding	every 5 min	when sounding
Fog implementation	**no**	**yes**	**no**	**yes**	**no**	**yes**
Time	7-17 UTC	4 -7 UTC	7-17 UTC	4 -7 UTC	7-17 UTC	4 -7 UTC
$I_{SolarAOT^{upper}}$	25.5	24.9	5.4	3.4	-	7.3
$I_{SolarAOT^{lower}}$	22.9	22.7	10.4	13.3	-	10.7
$I_{SolarAOT^{lower}}$ (-cirrus bias)	18.0	22.4				
Time	10-14 UTC	0 -7 UTC	10-14 UTC	0 -7 UTC		0 -7 UTC
$IR_{SolarAOT^{upper}}$	22.8	12.0	25.4	6.0	-	9.2
$IR_{SolarAOT^{lower}}$	20.8	12.1	22.5	12.6	-	19.9

Table 2. Statistics of SW (I) and LW (IR) flux comparison between model and observation at both sites. The MBE (mean bias error between model and observation) and RMSE were calculated for each day and for fog and non-fog conditions. In addition, for September 9 the mean MBE and RMSE for the SW radiation was calculated with removed estimated cirrus bias.

545 droplet radii. However in this study, were we exanimate fog conditions, the observed changes of LWC were mostly associated with the variation of N_c. This means that the change of LWC is mostly associated with the activation of fog droplets on the new nuclei than with growth by collision-coalescence process. Similar results were obtained by Okita (1962); Egli et al. (2015), which also studied vertical distribution of microphysical properties in radiation fogs. In three presented cases of radiation fog over Strzyżów valley we obtained that the effective radius (r_{eff}) is dropping with height. This is in line with Okita (1962) and
550 partially with observations of Egli et al. (2015) (in his study r_{eff} was dropping with height for some observations but mostly was constant with height). With the development of fog the decrease of r_{eff} with height is less pronounce but still visible.

In work of Okita (1962) big droplets are mostly concentrated near the ground (the volume radius of big droplets decrease with height). In our study drops larger than 18.5 μm appear in the spectrum. DSD with small concentrations of drops grater than 30 μm were observed in experiments conducted by Wendish et al. (1998); Gultepe et al. (2009); Mazoyer et al. (2022).

https://doi.org/10.5194/egusphere-2024-4074
Preprint. Discussion started: 17 February 2025

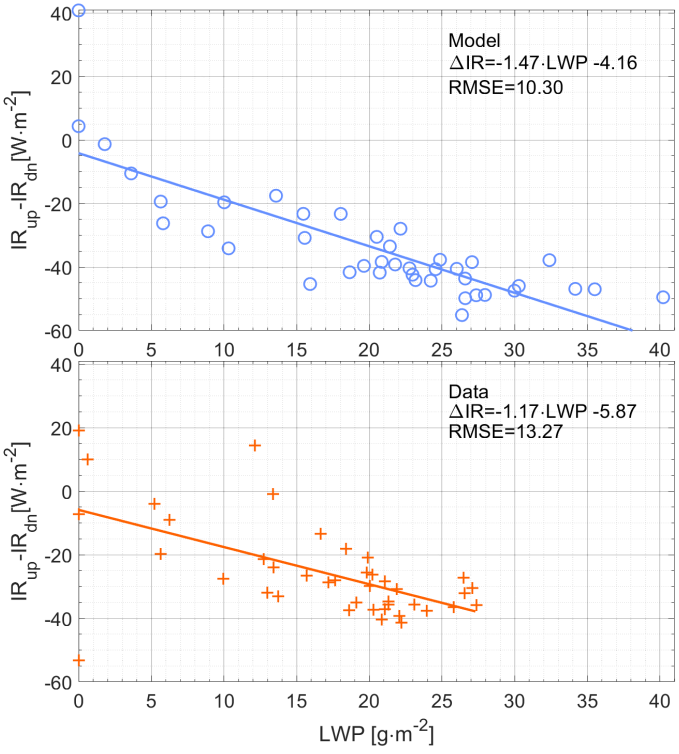

Figure 15. Relation between fog LWP (for days 8-11 September 2023) and the difference of LW downwards flux between the upper and lower SolarAOT stations. The upper panel presents the radiation transfer model simulations and the lower panel corresponds to the balloon profiles (LWP) and to radiometer observation at upper and lower SolarAOT station.

Those big droplets are the result of collision coalescence and Ostwald ripening processes. In presented study the volume of water is contained in two ranges of droplet radii. One is around 4-5 μm and the other is above 18.5μm. Even though droplets of radii grater than 18.5 μm are rare, the amount of water carried by them is significant. The significance of the first range increases with height, while of the second range decreases with height.

Simulations of numerical weather prediction (NWP) and large eddy simulations (LES) are predominantly based on bulk parametrization of e.g. LWP and N_c Bergot et al. (2007); Khain et al. (2015). For improved NWP and LES simulations of fog formation and dissipation, it is essential to incorporate the droplet spectrum across the fog layer Thoma et al. (2011). This would enable the removal of larger droplets through sedimentation, potentially alleviating the issue of excessively high LWC in fog forecasts Philip et al. (2016); Pithani et al. (2019).

In analyzed three cases the fog is disappearing from top and bottom. In mature stage the profile of LWC and N_c is growing with height and then after reaching maximum value decreasing to fog top height (CTH). During the decreasing stage region above the maximum N_c/LWC is squeezed. The maximum N_c/LWC is located above 80% of fog height. At the bottom of the fog the smallest droplets evaporate. As there is no production of new droplets, the big droplets are falling down and are

https://doi.org/10.5194/egusphere-2024-4074
Preprint. Discussion started: 17 February 2025

located mostly near to the ground, which reflects in r_{eff} higher at the bottom of the fog. Droplets of radius up to 40 μm can be described by an approximate formula for terminal velocity (u):

$$u(r) = k_1 \cdot r^2, \tag{25}$$

where $k_1 \approx 1.19 \cdot 10^6$ cm^{-1}·s^{-1} Yau and Rogers (1996). Using this formula, the fall velocity for drops larger than 18.5 μm is 4.07 cm/s. In the absence of droplet growth and turbulence, for example drops with radius 18.5 μm will be removed within 7 minutes from a fog of height 100 m. In the case of soundings through the final stage of the fog life cycle, no large drops are observed because they have been washed away.

In the article we calculated the theoretical equivalent adiabaticity (α_{eq}). The values of α_{eq} were in between 0.0 - 0.6, similarly to previous values reported for fog events. During one case at the begging stage of fog the negative value of α_{eq} was observed (-3.2). The elevated negative value was caused by high LWC value at the ground. In literature events were LWC decrease with height in fog were rarely observed Costabloz et al. (2024); Okita (1962); Boutle et al. (2018) and as well associated with thin fog with CTH not exceeding 40 m.

For studied cases the average fog core LWC was between 0.2-0.4 g·m^{-3}. LWC was increasing from ground to approximately 60% CTH height and than decreasing to CTH. The mean N_c was up to 300 cm^{-3}. In two fog cases (Night 08-09 and 09-10 September) the mean N_c with height could be approximated by a parabola curve. In the last fog case (10-11 September) the N_c had two local maxima at 25% and 88% of CTH. The mean r_{eff} in all cases was around 8-10 μm and was linearly decreasing with height. In Strzyżów location are mounted solar and infrared radiometers on two different heights (in fog and above it), which allows for determining the impact of fog on radiation fluxes. It has been shown that there is a negative correlation (for modeled data -0.81 and for observation -0.59) between the difference in infrared radiation and the total water content in the fog. The fog disappearing can drastically change the total radiation fluxes at the ground within a period of 10-30 min. by up to 160 W·m^{-2}.

During fog, the mean bias between observed and modeled radiation flux is around 2 W·m^{-2} for SW and 8 W·m^{-2} for LW at the lower station. The good agreement of radiative fluxes indicates the consistency of the measurement data on the physical properties of the fog.

Code and data availability. The data used in this article were uploaded to the repository. Nurowska, Katarzyna, 2024, "Microphysical and optical data of radiation fog in Strzyżów Valley, Poland", https://danebadawcze.uw.edu.pl/privateurl.xhtml?token=30df09f8-ce75-4c28-83ee-53bdc1b1c4fc, Dane Badawcze UW, V1.

Author contributions. K.N - Conceptualization, Methodology, Formal analysis, Investigation, Writing — original draft preparation, Writing—review and editing, Visualization; P.M. - lidar data visualisation; K.M. - Conceptualization, Supervision; All authors have read and agreed to the published version of the manuscript.

https://doi.org/10.5194/egusphere-2024-4074
Preprint. Discussion started: 17 February 2025

Competing interests. The authors declare no conflict of interest.

Acknowledgements. We thank the AERONET team, principal investigators and other participants for theirs effort in establishing and maintaining the network. This research is part of the OPUS project (Polish Grant No. 2017/27/B/ST10/00549) *Impact of aerosol on the microphysical, optical and radiation properties of fog*, which was funded by the National Science Centre coordinated by the Institute of Geophysics, Faculty of Physics, University of Warsaw.

List of abbreviations:

Abbreviation	**Description**	**Abbreviation**	**Description**
AE	aerosol Angstrom exponent	MSE	mean bias error
α_{eq}	theoretical equivalent adiabaticity	MWR	microwave radiometer
AOD	aerosol optical depth	NTSB	American National Transportation Safety Board
ASC_{525}	aerosol scattering coefficient of light at 525 nm	LES	large eddy simulations
CCN	cloud condensation nuclei	LW	longwave radiation
CTH	cloud / fog top height	LWC	liquid water content
DSD	droplet size distribution	LWC_0	non-zero surface liquid water content
eBC	equivalent of black carbon	LWP	liquid water path
N_c	droplet number concentration	RH	relative humidity
NC	particle number concentration	RMSE	root mean square error
NWP	numerical weather prediction	SBL	stable boundary layer
p	pressure	SSA	aerosol single scattering albedo
PM	particle matter	SW	shortwave radiation
r_{eff}	effective radius	T	temperature
RH	relative humidity	vDSD	volume droplet size distribution

https://doi.org/10.5194/egusphere-2024-4074
Preprint. Discussion started: 17 February 2025

References

Antoine, S., Honnert, R., Seity, Y., Vié, B., Burnet, F., and Martinet, P.: Evaluation of an Improved AROME Configuration for Fog Forecasts during the SOFOG3D Campaign, Weather and Forecasting, 38, 1605 – 1620, https://doi.org/10.1175/WAF-D-22-0215.1, 2023.

Bari, D., Bergot, T., and Tardif, R.: Fog Decision Support Systems: A Review of the Current Perspectives, Atmosphere, 14, https://doi.org/10.3390/atmos14081314, 2023.

Bergot, T., Terradellas, E., Cuxart, J., Mira, A., Leichti, O., Mueller, M., and Nielsen, N. W.: Intercomparison of single-column numerical models for the prediction of radiation fog, Journal of Applied Meteorology and Climatology, 46, 504 – 521, https://doi.org/10.1175/JAM2475.1, cited by: 87; All Open Access, Bronze Open Access, 2007.

Bergot, T., Escobar, J., and Masson, V.: Effect of small-scale surface heterogeneities and buildings on radiation fog: Large-eddy simulation study at Paris–Charles de Gaulle airport, Quarterly Journal of the Royal Meteorological Society, 141, 285–298, https://doi.org/https://doi.org/10.1002/qj.2358, 2015.

Betts, A. K.: Cloud Thermodynamic Models in Saturation Point Coordinates, Journal of Atmospheric Sciences, 39, 2182 – 2191, https://doi.org/10.1175/1520-0469(1982)039<2182:CTMISP>2.0.CO;2, 1982.

Boutle, I., Price, J., Kudzotsa, I., Kokkola, H., and Romakkaniemi, S.: Aerosol–fog interaction and the transition to well-mixed radiation fog, Atmospheric Chemistry and Physics, 18, 7827–7840, https://doi.org/10.5194/acp-18-7827-2018, 2018.

Boutle, I., Angevine, W., Bao, J.-W., Bergot, T., Bhattacharya, R., Bott, A., Ducongé, L., Forbes, R., Goecke, T., Grell, E., Hill, A., Igel, A. L., Kudzotsa, I., Lac, C., Maronga, B., Romakkaniemi, S., Schmidli, J., Schwenkel, J., Steeneveld, G.-J., and Vié, B.: Demistify: a large-eddy simulation (LES) and single-column model (SCM) intercomparison of radiation fog, Atmospheric Chemistry and Physics, 22, 319–333, https://doi.org/10.5194/acp-22-319-2022, 2022.

Brenguier, J. L.: Parameterization of the Condensation Process: A Theoretical Approach, Journal of Atmospheric Sciences, 48, 264 – 282, https://doi.org/10.1175/1520-0469(1991)048<0264:POTCPA>2.0.CO;2, 1991.

Brenguier, J.-L., Pawlowska, H., Schüller, L., Preusker, R., Fischer, J., and Fouquart, Y.: Radiative Properties of Boundary Layer Clouds: Droplet Effective Radius versus Number Concentration, Journal of the Atmospheric Sciences, 57, 803 – 821, https://doi.org/10.1175/1520-0469(2000)057<0803:RPOBLC>2.0.CO;2, 2000.

Capobianco, G. and Lee, M. D.: The Role of Weather in General Aviation Accidents: An Analysis of Causes, Contributing Factors and ISSUES, Proceedings of the Human Factors and Ergonomics Society Annual Meeting, 45, 190–194, https://doi.org/10.1177/154193120104500241, 2001.

Cermak, J. and Bendix, J.: Detecting ground fog from space – a microphysics-based approach, International Journal of Remote Sensing, 32, 3345–3371, https://doi.org/10.1080/01431161003747505, 2011.

Chang, F.-L. and Li, Z.: Estimating the vertical variation of cloud droplet effective radius using multispectral near-infrared satellite measurements, Journal of Geophysical Research: Atmospheres, 107, AAC 7–1–AAC 7–12, https://doi.org/https://doi.org/10.1029/2001JD000766, 2002.

Costabloz, T., Burnet, F., Lac, C., Martinet, P., Delanoë, J., Jorquera, S., and Fathalli, M.: Vertical Profiles of Liquid Water Content in fog layers during the SOFOG3D experiment, EGUsphere, 2024, 1–45, https://doi.org/10.5194/egusphere-2024-1344, 2024.

Egli, S., Maier, F., Bendix, J., and Thies, B.: Vertical distribution of microphysical properties in radiation fogs — A case study, Atmospheric Research, 151, 130–145, https://doi.org/https://doi.org/10.1016/j.atmosres.2014.05.027, sixth International Conference on Fog, Fog Collection and Dew, 2015.

https://doi.org/10.5194/egusphere-2024-4074
Preprint. Discussion started: 17 February 2025

Fu, Q. and Liou, K. N.: On the Correlated k-Distribution Method for Radiative Transfer in Nonhomogeneous Atmospheres, Journal of Atmospheric Sciences, 49, 2139 – 2156, https://doi.org/10.1175/1520-0469(1992)049<2139:OTCDMF>2.0.CO;2, 1992.

Fu, Q. and Liou, K. N.: Parameterization of the Radiative Properties of Cirrus Clouds, Journal of Atmospheric Sciences, 50, 2008 – 2025, https://doi.org/10.1175/1520-0469(1993)050<2008:POTRPO>2.0.CO;2, 1993.

George, J. J.: Fog, pp. 1179–1189, American Meteorological Society, Boston, MA, ISBN 978-1-940033-70-9, https://doi.org/10.1007/978-1-940033-70-9_95, 1951.

Gilardoni, S., Massoli, P., Giulianelli, L., Rinaldi, M., Paglione, M., Pollini, F., Lanconelli, C., Poluzzi, V., Carbone, S., Hillamo, R., Russell, L. M., Facchini, M. C., and Fuzzi, S.: Fog scavenging of organic and inorganic aerosol in the Po Valley, Atmospheric Chemistry and Physics, 14, 6967–6981, https://doi.org/10.5194/acp-14-6967-2014, 2014.

Gultepe, I.: A Review on Weather Impact on Aviation Operations: Visibility, Wind, Precipitation, Icing, Journal of Airline Operations and Aviation Management, 2, https://doi.org/10.5194/amt-16-2455-2023, 2023.

Gultepe, I., Pearson, G., Milbrandt, J. A., Hansen, B., Platnick, S., Taylor, P., Gordon, M., Oakley, J. P., and Cober, S. G.: The Fog Remote Sensing and Modeling Field Project, Bulletin of the American Meteorological Society, 90, 341 – 360, https://doi.org/10.1175/2008BAMS2354.1, 2009.

Gultepe, I., Sharman, R., and et all.: A Review of High Impact Weather for Aviation Meteorology., Pure Appl. Geophys., 176, 1869–1921, https://doi.org/10.1007/s00024-019-02168-6, 2019.

Hagan, D. H. and Kroll, J. H.: Assessing the accuracy of low-cost optical particle sensors using a physics-based approach, Atmospheric Measurement Techniques, 13, 6343–6355, https://doi.org/10.5194/amt-13-6343-2020, 2020.

Han, S.-Q., Hao, T.-Y., Zhang, M., Yao, Q., Liu, J.-L., Cai, Z.-Y., and Li, X.-J.: Observation Analysis on Microphysics Characteristics of Long-lasting Severe Fog and Haze Episode at Urban Canopy Top, Aerosol and Air Quality Research, 18, 2475–2486, https://doi.org/10.4209/aaqr.2017.10.0416, 2018.

Khain, A. P., Beheng, K. D., Heymsfield, A., Korolev, A., Krichak, S. O., Levin, Z., Pinsky, M., Phillips, V., Prabhakaran, T., Teller, A., van den Heever, S. C., and Yano, J.-I.: Representation of microphysical processes in cloud-resolving models: Spectral (bin) microphysics versus bulk parameterization, Reviews of Geophysics, 53, 247–322, https://doi.org/https://doi.org/10.1002/2014RG000468, 2015.

Lakra, K. and Avishek, K.: A review on factors influencing fog formation, classification, forecasting, detection and impacts, Rendiconti Lincei. Scienze Fisiche e Naturali, 33, 319–353, 2022.

Maronga, B. and Bosveld, F. C.: Key parameters for the life cycle of nocturnal radiation fog: a comprehensive large-eddy simulation study, Quarterly Journal of the Royal Meteorological Society, 143, 2463–2480, https://doi.org/https://doi.org/10.1002/qj.3100, 2017.

Mason, J.: The Physics of Radiation Fog, Journal of the Meteorological Society of Japan. Ser. II, 60, 486–499, https://doi.org/10.2151/jmsj1965.60.1_486, 1982.

Mazoyer, M., Lac, C., Thouron, O., Bergot, T., Masson, V., and Musson-Genon, L.: Large eddy simulation of radiation fog: impact of dynamics on
the fog life cycle, Atmospheric Chemistry and Physics, 17, 13 017–13 035, https://doi.org/10.5194/acp-17-13017-2017, 2017.

Mazoyer, M., Burnet, F., and Denjean, C.: Experimental study on the evolution of droplet size distribution during the fog life cycle, Atmospheric Chemistry and Physics, 22, 11 305–11 321, https://doi.org/10.5194/acp-22-11305-2022, 2022.

Mohammadi, M., Nowak, J. L., Bertens, G., Moláček, J., Kumala, W., and Malinowski, S. P.: Cloud microphysical measurements at a mountain observatory: comparison between shadowgraph imaging and phase Doppler interferometry, Atmospheric Measurement Techniques, 15, 965–985, https://doi.org/10.5194/amt-15-965-2022, 2022.

https://doi.org/10.5194/egusphere-2024-4074
Preprint. Discussion started: 17 February 2025

Nowak, J. L., Mohammadi, M., and Malinowski, S. P.: Applicability of the VisiSize D30 shadowgraph system for cloud microphysical measurements, Atmospheric Measurement Techniques, 14, 2615–2633, https://doi.org/10.5194/amt-14-2615-2021, 2021.

Nurowska, K., Mohammadi, M., Malinowski, S., and Markowicz, K.: Applicability of the low-cost OPC-N3 optical particle counter for microphysical measurements of fog, Atmospheric Measurement Techniques, 16, 2415–2430, https://doi.org/10.5194/amt-16-2415-2023, 2023.

Okita, T.: Observations of the vertical structure of a stratus cloud and radiation fogs in relation to the mechanism of drizzle formation, Tellus, 14, 310–322, https://doi.org/10.3402/tellusa.v14i3.9556, 1962.

Philip, A., Bergot, T., Bouteloup, Y., and Bouyssel, F.: The Impact of Vertical Resolution on Fog Forecasting in the Kilometric-Scale Model AROME: A Case Study and Statistics, Weather and Forecasting, 31, 1655 – 1671, https://doi.org/10.1175/WAF-D-16-0074.1, 2016.

Pinnick, R. G., Hoihjelle, D. L., Fernandez, G., Stenmark, E. B., Lindberg, J. D., Hoidale, G. B., and Jennings, S. G.: Vertical Structure in Atmospheric Fog and Haze and Its Effects on Visible and Infrared Extinction, Journal of Atmospheric Sciences, 35, 2020 – 2032, https://doi.org/10.1175/1520-0469(1978)035<2020:VSIAFA>2.0.CO;2, 1978.

Pithani, P., Ghude, S., Naidu, c., Kulkarni, R., Steeneveld, G.-J., Sharma, A., Prabha, T., Chate, D., Gultepe, I., Jenamani, R., and Rajeevan, M.: WRF model Prediction of a dense fog event occurred during Winter Fog Experiment (WIFEX), Pure and Applied Geophysics, 176, 1827–1846, https://doi.org/10.1007/s00024-018-2053-0, 2019.

Poku, C., Ross, A. N., Hill, A. A., Blyth, A. M., and Shipway, B.: Is a more physical representation of aerosol activation needed for simulations of fog?, Atmospheric Chemistry and Physics, 21, 7271–7292, https://doi.org/10.5194/acp-21-7271-2021, 2021.

Price, J.: Radiation Fog. Part I: Observations of Stability and Drop Size Distributions, Boundary-Layer Meteorology, 139, 167–191, https://doi.org/10.1007/s10546-010-9580-2, 2011.

Román-Cascón, C., Yagüe, C., Sastre, M., Maqueda, G., Salamanca, F., and Viana, S.: Observations and WRF simulations of fog events at the Spanish Northern Plateau, Advances in Science and Research, 8, 11–18, https://doi.org/10.5194/asr-8-11-2012, 2012.

Thoma, C., Schneider, W., Masbou, M., and Bott, A.: Integration of Local Observations into the One Dimensional Fog Model PAFOG, Pure and Applied Geophysics, 169, 881–893, https://doi.org/10.1007/s00024-011-0357-4, 2011.

Toledo, F., Haeffelin, M., Wærsted, E., and Dupont, J.-C.: A new conceptual model for adiabatic fog, Atmospheric Chemistry and Physics, 21, 13 099–13 117, https://doi.org/10.5194/acp-21-13099-2021, 2021.

Wærsted, E. G., Haeffelin, M., Dupont, J.-C., Delanoë, J., and Dubuisson, P.: Radiation in fog: quantification of the impact on fog liquid water based on ground-based remote sensing, Atmospheric Chemistry and Physics, 17, 10 811–10 835, https://doi.org/10.5194/acp-17-10811-2017, 2017.

Wendish, M., Mertes, S., Heintzenberg, J., Wiedensohler, A., Schell, D., Wobrock, W., Frank, G., Martinsson, B. G., Fuzzi, S., Orsi, G., Kos, G., and Berner, A.: Drop size distribution and LWC in Po valley fog, Contributions to Atmospheric Physics, 71, 87 – 100, https://www.scopus.com/inward/record.uri?eid=2-s2.0-0031779779&partnerID=40&md5=9b5423094749ae926835f315751c4503, cited by: 47, 1998.

Yau, M. and Rogers, R.: A Short Course in Cloud Physics, Elsevier Science, ISBN 9780080570945, https://books.google.pl/books?id=ClKbCgAAQBAJ, 1996.

Ye, X., Wu, B., and Zhang, H.: The turbulent structure and transport in fog layers observed over the Tianjin area, Atmospheric Research, 153, 217–234, https://doi.org/https://doi.org/10.1016/j.atmosres.2014.08.003, 2015.

Zhou, B., Du, J., Gultepe, I., and Dimego, G.: Forecast of Low Visibility and Fog from NCEP: Current Status and Efforts, Pure and Applied Geophysics, 169, 895–909, https://doi.org/10.1007/s00024-011-0327-x, 2012.

https://doi.org/10.5194/egusphere-2024-4074
Preprint. Discussion started: 17 February 2025

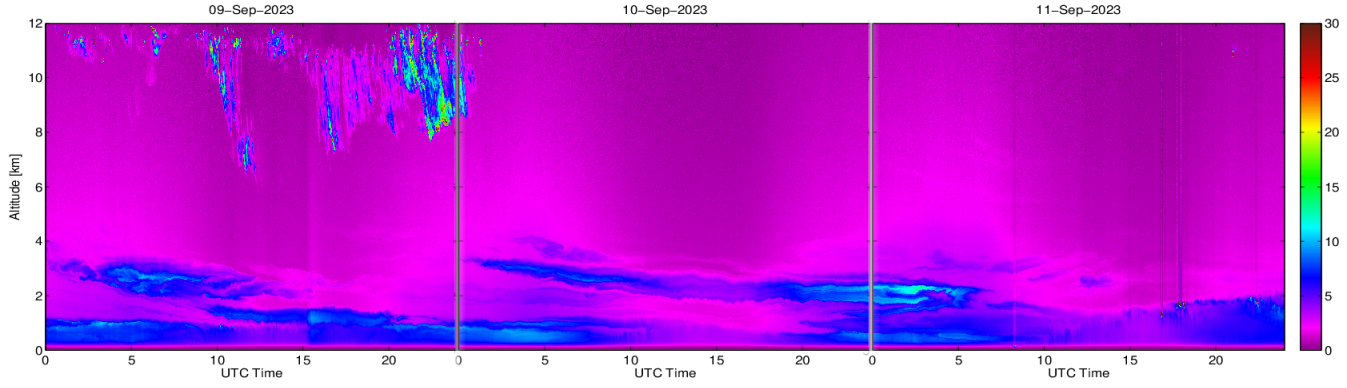

Figure A1. Temporal variability of 510M lidar range corrected signal (at 532 nm) from level of the upper station up to 12 km between 9 and 11 September 2023.

Appendix A: Temperature set up in the model

The data about T and RH where taken from HYT and GY-63 and interpolated to levels of model. As the measurements where mostly reaching 115 m, above the T and humidity profile were set according to the measurement from atmospheric sounding from Tarnów (WMO station 12575) done by IMGW (Polish Institute of Meteorology and Water Management). Tarnów is 60 km in straight line from Strzyżów city. For better description of the merging of data sounding from Tarnów will be called soundingT.

To have a smooth transition between balloon sounding and the soundingT the data from the balloon and soundingT were stitched together. For this purpose first the points were extrapolated so that at the stitching point the values from both soundings were available. The procedure was performed for the last three points (highest points) from the balloon profile and first two points of soundingT above balloon profile. Then for these five points the average value weighted by the distance of the points was taken. As the soundingT not always reach 10km, above soundingT the standard atmosphere profile for mid-latitude summer was used.

As profile of RH was stitched and interpolated, the precipitable water (PW) was changed. To fix this issue, the whole profile of RH has been rescaled in such a way that PW is the same as the PW obtained from soundingT before interpolating.

Appendix B: Additional Tables and Figures

https://doi.org/10.5194/egusphere-2024-4074
Preprint. Discussion started: 17 February 2025

sounding nr	Day	Time	Radiosonde	AE-51	GY63	HYT	OPC-N3	SPS30	sounding nr	Day	Time	Radiosonde	AE-51	GY63	HYT	OPC-N3	SPS30	sounding nr	Day	Time	Radiosonde	AE-51	GY63	HYT	OPC-N3	SPS30
1	08	20:29 - 20:42	□						28	09	17:59 - 18:10	●	●					54	11	02:11 - 02:17			►	►	►	►
2	08	21:00 - 21:35	□						29	10	00:41 - 00:51			□	□	□	□	55	11	02:19 - 02:26			□	□	□	□
3	08	22:24 - 22:34			□	□	□	□	30	10	00:53 - 01:05	●						56	11	02:29 - 02:37			□	□	□	□
4	09	00:22 - 00:28			►	►	►	►	31	10	01:18 - 01:28			□	□	□	□	57	11	02:43 - 03:02	●					
5	09	00:30 - 00:40			►	►	►	►	32	10	01:37 - 01:46			□	□	□	□	58	11	03:10 - 03:20			►	►	►	►
6	09	00:48 - 01:01	●						33	10	01:55 - 02:04	●						59	11	03:23 - 03:33			►	►	►	►
7	09	01:20 - 01:27			►	►	►	►	34	10	02:24 - 02:34			►	►	►	►	60	11	03:36 - 03:46			►	►	►	►
8	09	01:32 - 01:41			►	►	►	►	35	10	02:40 - 02:48			►	►	►	►	61	11	03:49 - 03:59	●					
9	09	02:34 - 02:42			►	►	►	►	36	10	02:54 - 03:06			►	►	►	►	62	11	04:04 - 04:16			►	►	►	►
10	09	02:45 - 02:55			►	►	►	►	37	10	03:09 - 03:23	●						63	11	04:19 - 04:36			►	►	►	►
11	09	03:03 - 03:27	●						38	10	03:33 - 03:44			►	►	►	►	64	11	04:40 - 04:56			►	►	►	►
12	09	03:34 - 04:03			►	►	►	►	39	10	03:49 - 04:00			►	►	►	►	65	11	04:59 - 05:15	●					
13	09	04:09 - 04:22			►	►	►	►	40	10	04:06 - 04:17			►	►	►	►	66	11	05:19 - 05:30			►	►	►	►
14	09	05:10 - 05:21			►	►	►	►	41	10	04:20 - 04:40	●						67	11	05:32 - 05:45			►	►	►	►
15	09	05:23 - 05:34			►	►	►	►	42	10	04:50 - 05:00			►	►	►	►	68	11	05:47 - 05:59			►	►	►	►
16	09	05:37 - 05:45			►	►	►	►	43	10	05:06 - 05:21			►	►	►	►	69	11	06:02 - 06:11	●	●				
17	09	05:47 - 05:54	▲		▲	▲	▲	▲	44	10	05:25 - 05:37			►	►	►	►	70	11	06:18 - 06:33	●	●				
18	09	05:56 - 06:06	▲		▲	▲	▲	▲	45	10	05:40 - 05:56	●						71	11	06:39 - 06:53			►	►	►	►
19	09	06:09 - 06:17	▲		▲	▲	▲	▲	46	10	06:03 - 06:13			□	□	□	□	72	11	06:56 - 07:14	●	●				
20	09	06:19 - 06:28	▲		▲	▲	▲	▲	47	10	06:23 - 06:31			►	►	►	►	73	11	07:15 - 07:29	●	●				
21	09	06:33 - 06:42	▲		▲	▲	▲	▲	48	10	06:31 - 06:40			►	►	►	►	74	11	07:36 - 07:51	●	●				
22	09	06:45 - 06:53	▲		▲	▲	▲	▲	49	10	06:42 - 06:50	●	●													
23	09	06:56 - 07:03	▲		▲	▲	▲	▲	50	10	06:52 - 07:00			□	□	□	□									
24	09	07:07 - 07:13	▲		▲	▲	▲	▲	51	10	07:01 - 07:19	●	●													
25	09	07:18 - 07:41	●	●					52	10	07:11 - 07:17			□	□	□	□									
26	09	07:42 - 07:56	●	●					53	10	07:22 - 07:32	●	●													
27	09	07:57 - 08:08	●	●																							

Table A1. Apparatus used during each of the soundings of case study 8 - 11 September 2023. Markers represents: ► - setup with OPC-N3, ● - setup with radiosonde, ▲- setup with OPC-N3 and radiosonde, □ - problems with collected data (sounding with partially recorded data were not taken into further analysis.

https://doi.org/10.5194/egusphere-2024-4074
Preprint. Discussion started: 17 February 2025

Figure A2. Visualization of radiation fog top. Photos were taken with the camera at the SolarAOT^{upper} station at 4 UTC each day.

https://doi.org/10.5194/egusphere-2024-4074
Preprint. Discussion started: 17 February 2025

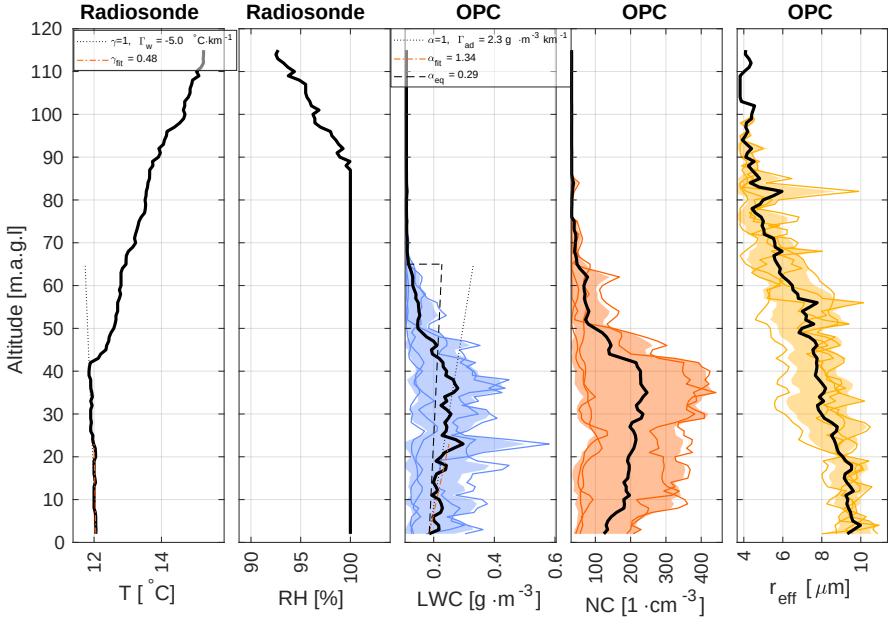

(a) Development stage of fog.

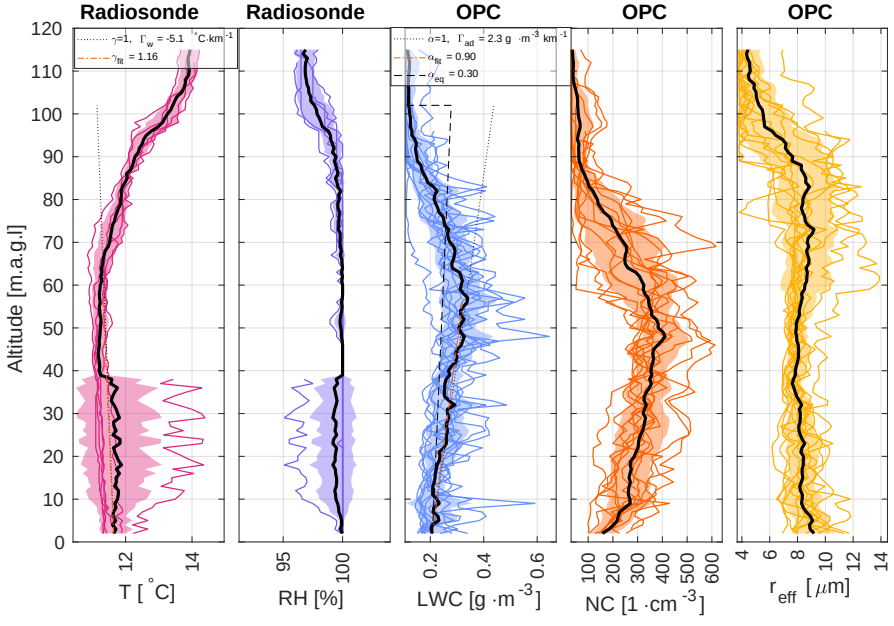

(b) Mature state of fog.

Figure A3. Figures presents specific quantities measured by the balloon for each stage of fog observed during night 08-09 Sep. 2023.

https://doi.org/10.5194/egusphere-2024-4074
Preprint. Discussion started: 17 February 2025

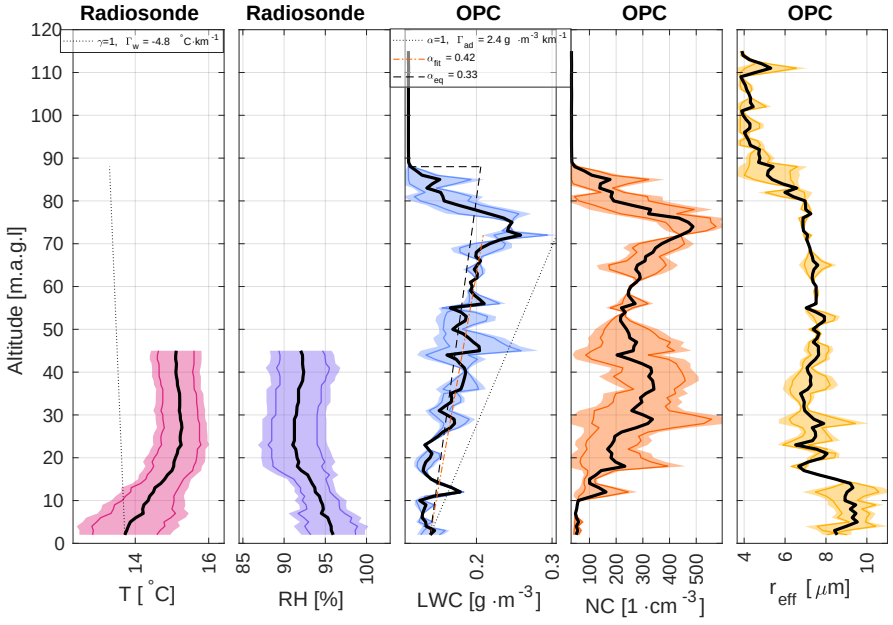

(c) Disappearing stage of fog

Figure A3. Figures presents specific quantities measured by the balloon for each stage of fog observed during night 08-09 Sep. 2023. From left: T from Vaisala radiosonde RS41, RH from Vaisala radiosonde RS41, N_c, r_{eff} within the fog. Each colored line represents one balloon profile. Black thick line represents the mean of all the soundings, colored area represents range in between +/- standard deviation from the mean. At the T plot dotted line presents the lapse rate, dashed red line presents the linear fit to T from 3 m to height of maximum mean LWC. At the LWC plot dotted line presents the LWC adiabatic lapse rate, dashed red line presents the linear fit to LWC from 3 m to height of maximum mean LWC.

https://doi.org/10.5194/egusphere-2024-4074
Preprint. Discussion started: 17 February 2025

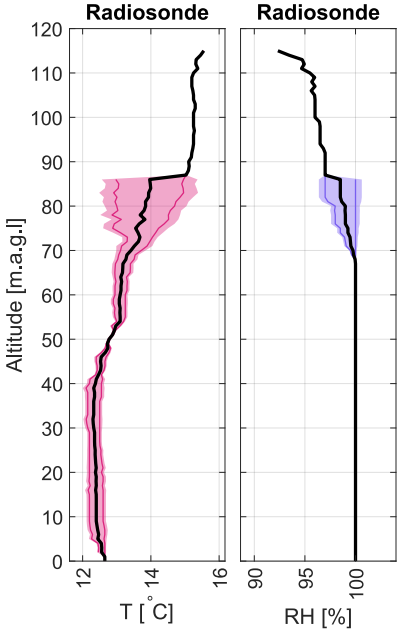

(a) Development stage of fog.

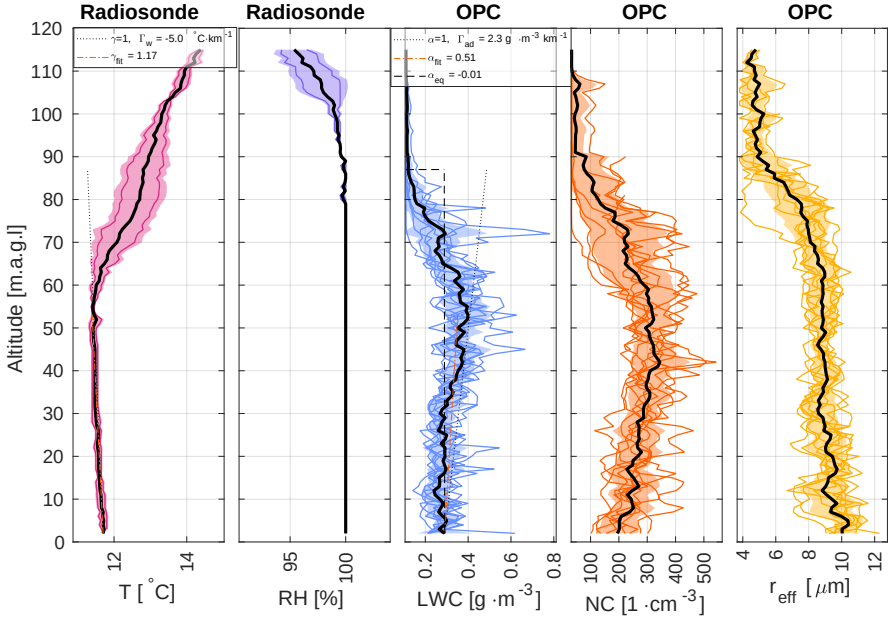

(b) Mature state of fog.

Figure A4. Figures presents specific quantities measured by the balloon for each stage of fog observed during night 10-11 Sep. 2023.

https://doi.org/10.5194/egusphere-2024-4074
Preprint. Discussion started: 17 February 2025

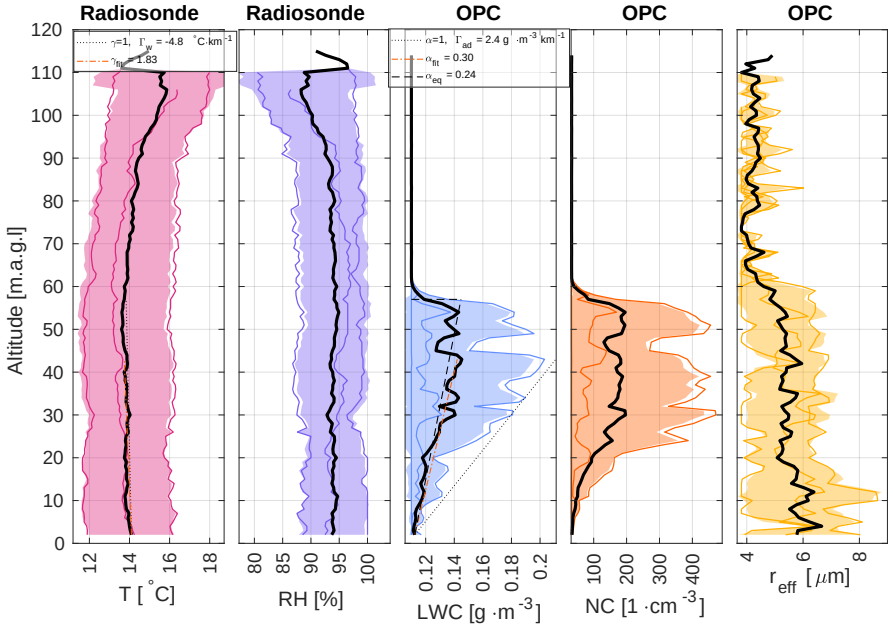

(c) Disappearing stage of fog

Figure A4. Figures presents specific quantities measured by the balloon for each stage of fog observed during night 09-10 Sep. 2023. From left: T from Vaisala radiosonde RS41, RH from Vaisala radiosonde RS41, N_c, r_{eff} within the fog. Each colored line represents one balloon profile. Black thick line represents the mean of all the soundings, colored area represents range in between +/- standard deviation from the mean. At the T plot dotted line presents the lapse rate, dashed red line presents the linear fit to T from 3 m to height of maximum mean LWC. At the LWC plot dotted line presents the LWC adiabatic lapse rate, dashed red line presents the linear fit to LWC from 3 m to height of maximum mean LWC.

https://doi.org/10.5194/egusphere-2024-4074
Preprint. Discussion started: 17 February 2025

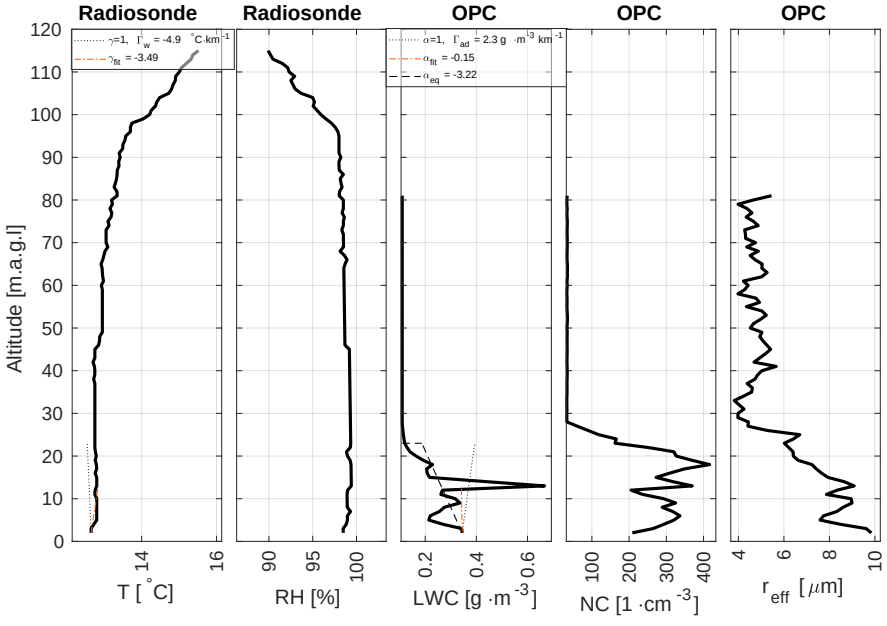

(a) Development stage of fog.

Figure A5. Figures presents specific quantities measured by the balloon for each stage of fog observed during night 10-11 Sep. 2023.

https://doi.org/10.5194/egusphere-2024-4074
Preprint. Discussion started: 17 February 2025

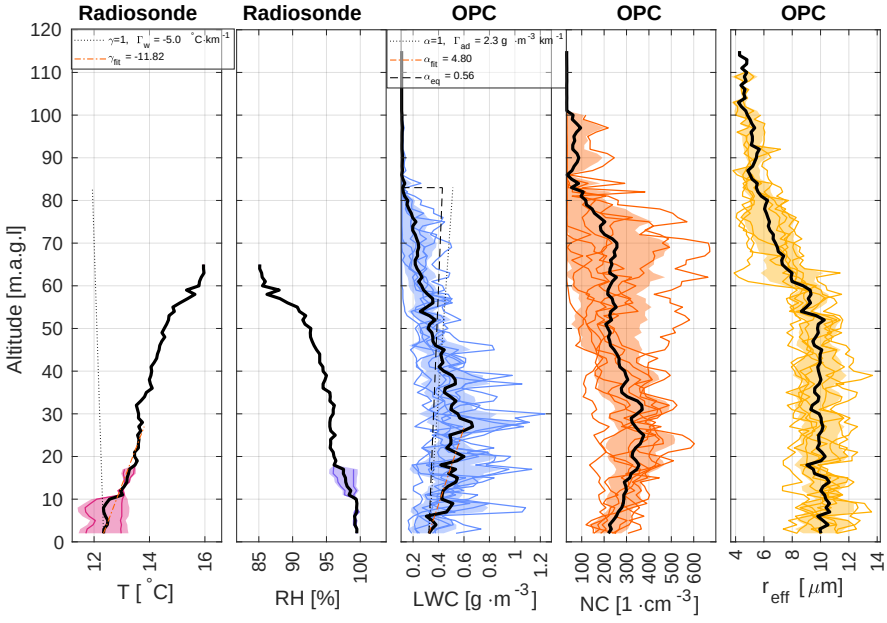

(b) Mature state of fog.

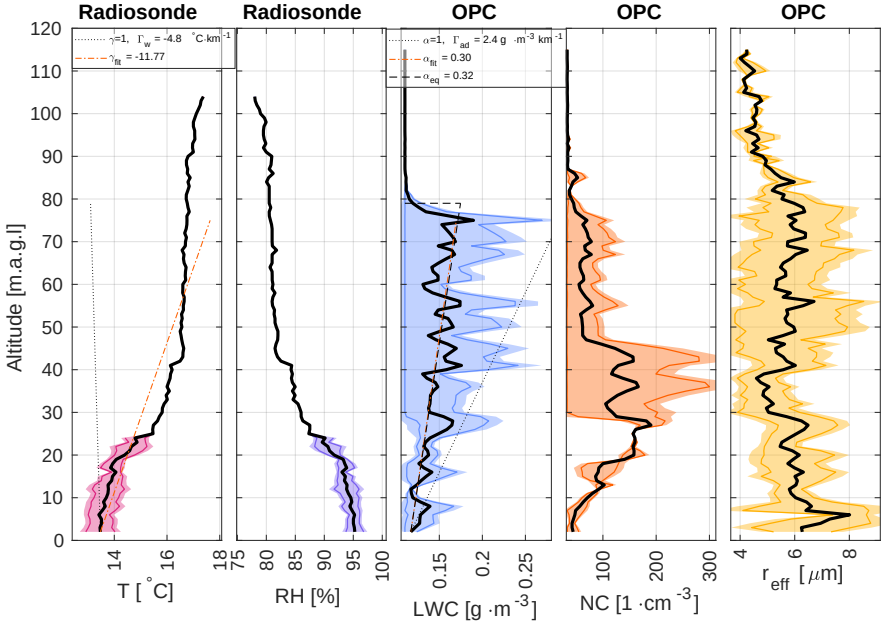

(c) Disappearing stage of fog

Figure A5. Figures presents specific quantities measured by the balloon for each stage of fog observed during night 10-11 Sep. 2023. From left: T from Vaisala radiosonde RS41, RH from Vaisala radiosonde RS41, N_c, r_{eff} within the fog. Each colored line represents one balloon profile. Black thick line represents the mean of all the soundings, colored area represents range in between +/- standard deviation from the mean. At the T plot dotted line presents the lapse rate, dashed red line presents the linear fit to T from 3 m to height of maximum mean LWC. At the LWC plot dotted line presents the LWC adiabatic lapse rate, dashed red line presents the linear fit to LWC from 3 m to height of maximum mean LWC.

https://doi.org/10.5194/egusphere-2024-4074
Preprint. Discussion started: 17 February 2025

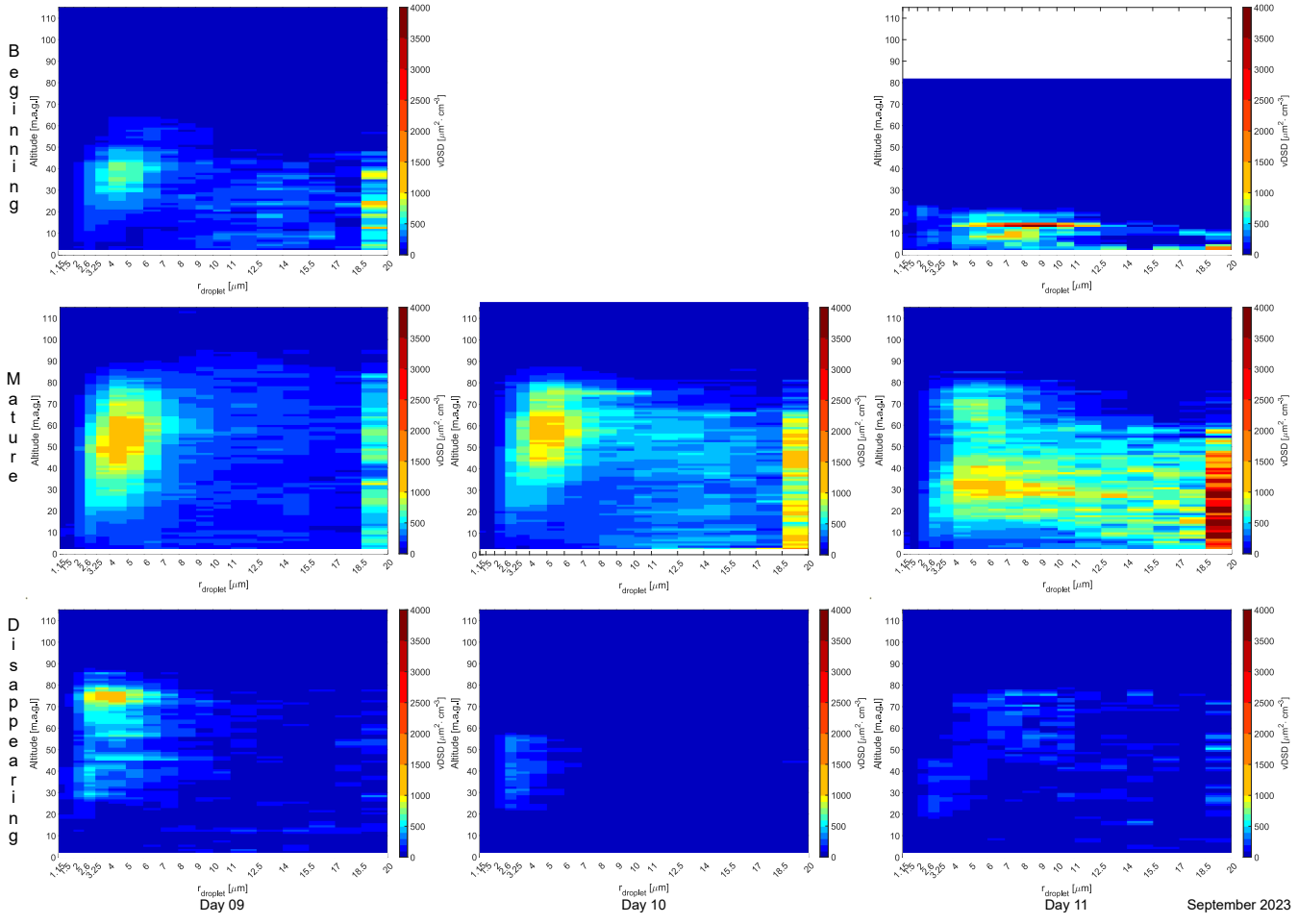

Figure A6. Profiles with height of vDSD for 8-11 September 2023 fog occurrence. In columns different days, in rows from top: beginning, mature and disappearing stage of fog.